Applied Catalysis B: Environmental xxx (xxxx) 122078

Contents lists available at ScienceDirect

Applied Catalysis B: Environmental

journal homepage: www.elsevier.com/locate/apcatb

Fischer-Tropsch synthesis over lignin-derived cobalt-containing porous carbon fiber catalysts

M.J. Valero-Romero [a, b], F.J. García-Mateos [a], Freek Kapteijn [b], J. Rodríguez-Mirasol [a, *], T. Cordero [a]

[a] Universidad de Málaga, Andalucía Tech, Escuela de Ingenierías Industriales, Campus de Teatinos s/n, 29010 Málaga, Spain
[b] Catalysis Engineering, Dept. Chemical Engineering, Delft University of Technology, Julianalaan 136, 2628 BL Delft, the Netherlands

ARTICLE INFO

Keywords:
Fischer-Tropsch synthesis
Lignin
Electrospinning
Co-containing carbon fibers

ABSTRACT

Cobalt-containing lignin-based fibers were synthesized in one step by electrospinning of Alcell lignin solutions as carbon precursor, a low-cost and renewable co-product of the paper making industry. The lignin fibers were thermostabilized in air to avoid the fusion during the carbonization process between 500 and 800 °C to obtain cobalt-containing porous carbon submicron fibers. These carbon fibers catalysts were studied for the Low-Temperature Fischer-Tropsch synthesis. The lignin-derived fibers containing Co catalyst located on the overall carbon fiber surface (internal and external) heat-treated at 500 °C (Co@CF-500) showed the best catalytic performance after 70 h on stream, with 75% and 60% selectivity to C5 + at 220 °C and H_2/CO ratios of 1 and 2, respectively, attributed to the high Co dispersion, optimal Co-particle size and better Co accessibility. Higher heat-treatment temperatures leaded to Co-containing carbon fibers with larger metallic cobalt nanoparticles encapsulated in graphitic-type carbon, which rendered them inaccessible for FTS.

1. Introduction

The growing concerns of greenhouse effects of using fossil resources has boosted research attention in finding sustainable alternative feedstocks for important petrochemical-based products. In this context, the development of efficient routes in the transformation of biomass to high quality clean hydrocarbon fuels and valuable chemicals is of primary importance. Among possible options for the valorization of biomass, gasification (followed by syngas conditioning and cleaning) [1] and Fischer–Tropsch synthesis (FTS) have received a renewed attention due to a mature gasification technology, increased concern on energy and the implementation of more stringent environmental legislations on liquid fuels [2,3]. Nowadays, however, gas to liquid (GTL) and carbon to liquid (CTL) technologies are only economically viable at large scales to meet the demand of oil fuel. Process intensification and catalyst design are both crucial steps to be optimized for the successful implementation of Biomass-to-liquid-Fischer-Tropsch (BTL-FT) processes for the valorization of biomass and the production of biofuels [1].

Supported cobalt nanoparticles (NPs) are frequently used as Low-Temperature Fischer–Tropsch synthesis (LT-FTS) catalyst (200–240 ºC) due to their efficiency for long-chain hydrocarbon synthesis and resistance to deactivation [4–6]. Here, both activity and selectivity of the process are strongly affected by the cobalt particle size and by and optimal utilization of the cobalt active phase (that requires to be in the metallic form under reaction conditions). Therefore, the control of metal loading, nanoparticle size, metal distribution, reducibility and accessibility have become a catalyst synthesis challenge because of the dependence between these performance parameters. A promising approach involves the use of carbon materials or carbon/ceramic composites as supports for FT catalysts since they can offer distinct advantages compared with oxides materials, such as higher resistance to acidic or basic media, higher thermal stability, lower metal-support interactions and higher metal-supported reducibility [7]. In addition to this, the high thermal conductivity of carbon materials has evidenced to favor the catalyst heat-transfer properties during the highly exothermic FTS reaction [7–9]. Different carbon-based materials have been widely used as supports for cobalt-based FT catalysts, such as activated carbons (Co/AC) [10–14], carbon nanotubes and nanofibers (Co/CNT and Co/CNF) [5,12,15–17], carbon spheres (Co/CS) [18], ordered mesoporous carbons (Co/CMK-3) [18,19] etc., and carbon/ceramic composites, such as Co/C-mesoHZSM-5 [20], Co/C-SiO_2 [21], Co/C-TiO_2 [22] and, most recently, Metal Organic Frameworks (MOFs) derived catalysts via the MOF-mediated synthesis route (Co@C) [23–26]. Most of these studies dealing with the use of carbon-based materials containing Co proposed the use of petroleum-derived compounds or induced graphitic carbon structures as carbon source. Nevertheless, less effort has been devoted

* Correspondence to: Universidad de Málaga, Departamento de Ingeniería Química, Campus de Teatinos, c/Doctor Ortiz Ramos s/n, 29071 Málaga, Spain.
E-mail address: mirasol@uma.es (J. Rodríguez-Mirasol).

https://doi.org/10.1016/j.apcatb.2022.122078
Received 29 June 2022; Received in revised form 11 October 2022; Accepted 13 October 2022
0926-3373/

about the use of lignocellulosic biomass residues as precursor of the carbonaceous FT catalyst support [7]. In this sense, biomass waste, besides being one of the feedstock to produce synthesis gas, can be used as carbon precursor for the preparation of the catalytic support, as well, due to the capacity and versatility of different lignocellulosic waste to produce carbonaceous materials with high specific surface area and tunable porous structure and surface chemistry during the preparation procedure [27]. The use of biomass waste for the preparation of the carbon support has an additional advantage, once the catalyst is exhausted at the end of its lifecycle, the supported metal active phase can be easily recovered by a gasification/oxidation step of the carbonaceous material, producing syngas (the feedstock of the FT process) and without net contribution to CO_2 emission.

In this regard, lignin is proposed in the present work as a renewable carbon precursor for the preparation of catalytic fibrillar support. Lignin is the second most abundant polymer in biomass after cellulose and it is generated mainly as a co-product in the papermaking industry. Among the different processes to obtain lignin, the Organosolv pulping process generates lignin soluble in non-toxic organic solvents, such as ethanol, with very low content in inorganic materials [28]. Biorefineries will be another important source of lignin in the near future [29]. On the other hand, the high carbon and aromatic content of lignin make it a very interesting carbon precursor for the preparation of porous carbon materials with high value added [30–32]. Carbon materials from lignocellulosic residues can be prepared in different conformations, powder, monoliths and submicro/nanofibers [30,33,34]. Particularly, structured fibrillar catalysts with submicron size have some advantages over other carbon conformations, such as adequate combination of high geometrical surface area, excellent mass and heat transfer properties, especially in such a highly exothermic reaction where heat management is challenging, low-pressure drop and good flexibility to fit into any reactor geometric design. Similarly, the small fiber diameter can make the diffusional limitations negligible [35]. Among the different technologies for the preparation of carbon fibers (CFs), electrospinning has emerged in recent years as a simple and versatile technique for the preparation of novel binderless lignin-based submicron CFs, using high voltage electrical fields and a spinnable precursor solution [30,36–39]. The properties of the CFs can be modulated by adding different heteroatoms to the initial lignin/ethanol solution and even ceramic/lignin composite fibers can be prepared instead, with a few modifications of the configuration set-up (coaxial and triaxial configurations)[40]. In the former case, metal-containing CFs can be obtained in a single step with very well dispersion of the heteroatom, which increases the dopant active surface of the catalyst [37–39]. Therefore, depending on the concentric needles configuration it is possible to design the catalyst to obtain simple mixed submicron fibers, in which the active phase can be located only on the external surface of the fiber or in the whole matrix (external and internal surface), depending of the fiber final application. The use of submicrometric fiber catalysts allows a better catalyst utilization with such a reduced particle size without compromising the pressure drop in a fixed-bed reactor, which may result in higher volumetric productivity, with shorter reactors and larger diameters and reduced danger of hot spots [41]. To our best knowledge, it is the first time that lignin-based CFs and the electrospinning technique are both used for the preparation of FTS catalysts.

In summary, we report a simple and versatile method to prepare a new, low-cost and renewable cobalt-containing lignin-based carbon fibers catalysts for LT-FTS. The preparation method involved the electrospinning of Cobalt nitrate/lignin/ethanol solutions into submicro-sized cobalt-containing lignin based fibers in a single step, where the FT catalytic active phase was deposited on the whole fiber matrix or only on the external surface of the fiber by using a coaxial configuration of the electrospinning set up. The lignin fibers were later stabilized in air to avoid the fusion during the pyrolysis process to obtain the carbon fibers, performed at different temperatures. The synthesis of lignin-derived CFs by the use of the electrospinning method has been reported previously [36,42,43]. Thus, in the present work the potential of lignin as precursor for the production of Co-containing CFs via electrospinning and their feasibility as catalysts for FTS with H_2/CO ratios of 2 and 1, being the latter comparable to that of the syngas from the gasification of biomass.

2. Experimental section

2.1. Preparation of cobalt-containing CFs

2.1.1. Materials

Alcell®lignin from organosolv process was purchased from Repap Technology Inc. In this process, ethanol is used as the delignifying agent and lignin is obtained as a sulfur-free, fine, brown powder (65.9 wt% C; 6.3 wt% H; 0.2 wt% N; 0.00 wt% S; and 27.6 wt% O, while the ash content was 0.00 wt%, according to its elemental analysis (PerkinElmer® 2400 C Instruments))[44]. $Co(NO_3)_2{\cdot}6H_2O$ (≥ 98%) and ethanol absolute (≥ 99.5%) were purchased form Sigma-Aldrich.

2.1.2. Electrospinning

Pure and Co-containing lignin fibers were prepared by electrospinning technique in a co-axial configuration, according to the experimental procedure described in Scheme 1. The coaxial electrospinning method for the preparation of pure lignin fibers is described in detail elsewhere [36]. Briefly, the co-axial electrospinning set-up, which is shown in Scheme 1 (Figure a), includes two coaxial needles in the spinneret connected to a high voltage power supply and separated at a short distance from a collector. A highly concentrated lignin solution to be spun is usually prepared using ethanol as solvent and pumped at a fixed flow rate through the spinneret via the inner needle (B), whereas ethanol is only pumped by the outer needle (A) to obtain pure lignin fibers (Approach 1). After applying a high voltage, between the spinneret and the collector, a typical Taylor cone is formed at the tip of the needle. By increasing the voltage, a liquid jet is issued that solidified during the flight by evaporation of the solvent and pure lignin fibers are produced on the collector. The purpose of flowing ethanol through the outermost capillary needle is to avoid the solidification of Taylor cone by the rapid evaporation of ethanol from the lignin solution, and thus allow the preparation of lignin fibers continuously [36,39]. An Alcell® lignin:ethanol solution with a weight ratio of 1:1 (solution B in Figure a of Scheme 1) was pumped by the internal needle and ethanol was used as a solvent (solution A in Figure a of Scheme 1) for the external one.

Scheme 1 also illustrates the catalysts synthetic procedures followed in the present work. Two different approaches were performed in order to prepare Co-containing carbon fibers catalysts, where Co nanoparticles were placed in the most external carbon fibers surface (Approach 2) or in the overall carbon structure (Approach 3). In the Approach 2, cobalt nitrate was dissolved in ethanol (solution A in Figure a of Scheme 1) and pumped through the outer needle, while for the internal one, a solution of Alcell® lignin:ethanol with a weight ratio of 1:1 (solution B in Figure a of Scheme 1) was pumped. In this case, the maximum cobalt nitrate:ethanol weight ratio used in the solution A to obtain a spinnable solution was 0.1:1. For the preparation of the cobalt-containing lignin fibers on the whole structure (Approach 3), a cobalt nitrate-lignin-ethanol solution with a weight ratio of 0.17:1:1 (solution B in Figure a of Scheme 1) was pumped through the inner needle, while ethanol (Solution A in Figure a of the Scheme 1) was used as solvent for the external one. The preparation of pure carbon fibers without Co in their structure (Approach 1) was used for comparison.

For pure lignin fibers, the applied electrical potential difference was 14 kV (the collector was at −7 kV and the tips at +7 kV). However, lignin fibers containing cobalt needed an electrical voltage of 12 kV (collector at – 6 kV and tip at + 6 kV) to form the Taylor cone due to

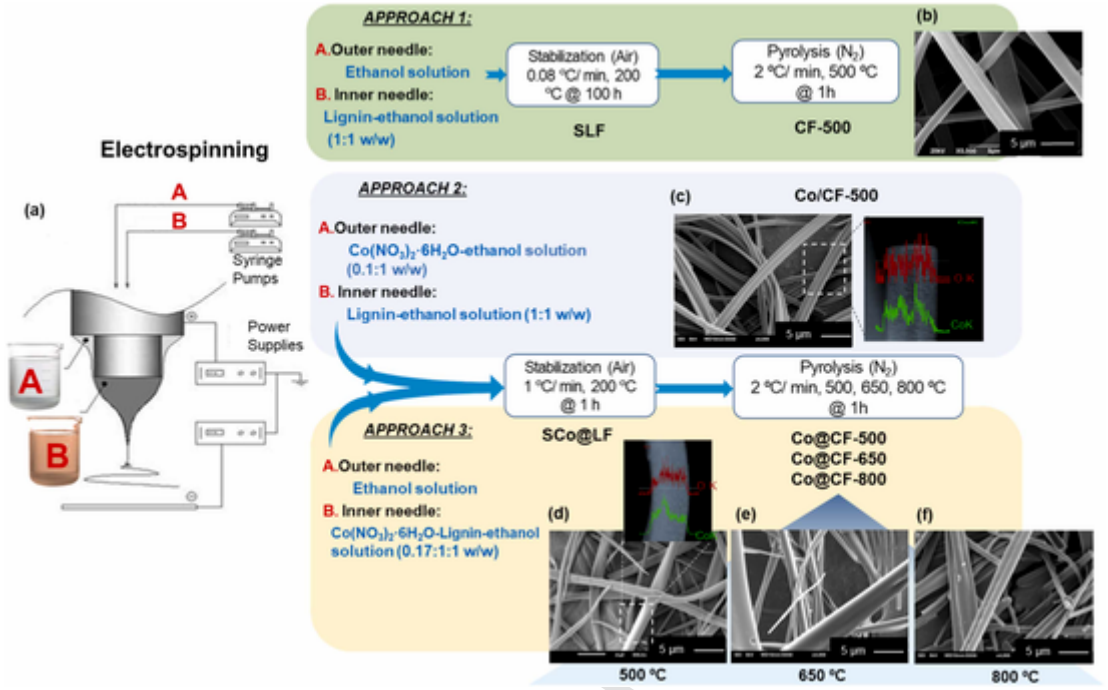

Scheme 1. Scheme of the preparation of cobalt-containing and pure carbon fiber by electrospinning of lignin solution: electrospinning system with coaxial needle configuration (a), SEM image of CF-500 (b), SEM image and EDX elemental mapping showing a line for cobalt and oxygen of Co/CF-500 (c) and SEM images of Co@CF-500 (d), Co@CF-650 (e) and Co@CF-800 (f).

electrostatic interactions caused by the cobalt nitrate. The ethanol and lignin solution flow rates were 0.1 and 1 mL h^{-1}, respectively, for the preparation of pure lignin fibers (Approach 1). For the Approach 2, the flow rates needed for cobalt nitrate and lignin solutions were 0.3 and 3 mL h^{-1}, respectively. In the case of the lignin solution containing cobalt nitrate (Approach 3), the flow rates needed were 0.15 mL h^{-1} for ethanol and 3 mL h^{-1} for lignin/cobalt nitrate solution. In all cases, the tip-to-collector distance was 25 cm.

2.1.3. Thermostabilization and heat treatment processes

The electrospun lignin and cobalt-lignin fibers were thermostabilized in air prior to the carbonization step in order to increase the glass transition temperature of lignin and thus avoid fibers from partial or total fusion. The electrospun pure fibers and the cobalt-lignin fibers were thermostabilized in an air flow (50 cm^3_{STP} min^{-1}) from 60 to 200 °C in an oven and with a heating rate of 0.08 and 1 °C min^{-1}, respectively, and maintained at the final temperature for 100 and 1 h, for pure and Co-containing lignin fibers, respectively. The stabilized lignin fibers and cobalt-containing lignin fibers were denoted as SLF (Approach 1) and SCo/LF (Approach 2) and SCo@LF (Approach 3), respectively. The stabilized samples were later heat treated in continuous N_2 flow (150 cm^3_{STP} min^{-1}) in a tubular furnace at different temperatures (500, 650 and 800 ºC) and at a heating rate of 2 °C min^{-1}, maintaining the final temperature for 1 h. Before exposition to ambient conditions, the samples were passivated in a flow (150 cm^3_{STP} min^{-1}) of 5 vol% O_2 in N_2 at room temperature for 2 h. The cobalt-containing carbon fibers were denoted as Co/CF-500 when cobalt is located on the external fiber surface (Approach 2), where the number indicates the pyrolysis temperature, and as Co@CF-T (where T = 500, 650 or 800 °C) when cobalt is located overall the carbon fiber structure (Approach 3). The pure lignin carbon fibers were denoted as CF-500 (Approach 1). Scheme 1 also summarizes the thermal treatment conditions and notation of the samples.

2.2. Characterization

The thermogravimetric analysis (TGA) of fresh and used samples was evaluated in a CI Electronics MK2 balance with 20 mg samples in an air flow (100 cm^3_{STP} min^{-1}) from room temperature up to 900 °C at a heating rate of 5 °C min^{-1}. The thermal decomposition of the SLF and SCoLF was also carried out in the thermogravimetric analyzer coupled with a mass spectrometer under purified helium (99.999%) flow and under similar heating conditions (TG/MS). The recorded m/z ratios (along with their assignations) were as follows: 2 (H_2), 4 (He), 16 (CH_4), 18 (H_2O), 28 (CO) and 44 (CO_2). The contribution of fragmented species on certain m/z lines was corrected by subtracting the relative fragmentation coefficient of single compounds.

The textural properties of the samples were measured by N_2 adsorption–desorption at − 196 °C and by CO_2 adsorption at 0 °C in a Micromeritics ASAP2020 unit. Before measurement, the samples were degassed at 150 °C for 8 h under 50 Torr. From the N_2 adsorption/desorption isotherm, the apparent surface area (S_{BET}) was determined from the BET equation [45] and the micropore volume (V_{micro}) and mesopore surface area (S_{meso}) by the *t*-method. The narrow micropore volume (V_{DR}) and the narrow micropore surface area (S_{DR}) were obtained by application of the Dubinin–Radushkevich (DR) equation to the CO_2 adsorption data [46]. The mesopore volume (V_{meso}) was calculated as the difference between the adsorbed volume of N_2 at a relative pressure of 0.95 (V_{total}) and the micropore volume (V_{micro}) [47]. Pore size distribution curves were obtained by the density functional theory (DFT) method applied to the N_2 adsorption data [48].

The Co content of the catalysts was measured by Inductively Coupled Plasma Optical Emission Spectrometry (ICP-OES) using a Perkin Elmer Optima instrument.

X-ray photoelectron spectroscopy (XPS) data was measured using a 5700 C model Physical Electronics apparatus with Mg-Kα radiation (1253.6 eV). Binding energy values were referred to the C_{1s} peak position set at 284.5 eV.

X-Ray Diffraction (XRD) patterns of the fresh catalysts (before in situ H_2 reduction) were measured by a Bruker D8 Advance X-ray dif-

fractometer using a monochromatic Co-Kα (λ = 0.179026 nm) radiation from 2θ = 10–70°. The samples were placed on a silica substrate and rotated during the measurements. The average crystal size of Co_3O_4 and Co in the catalysts were calculated according to Scherrer´s equation applied to the most intense diffractions (2θ = 43° and 51.8°, respectively) using a shape factor K = 0.9.

Raman spectra were acquired with a JASCO NRS-5100 Raman system using an Ar^+ laser at 785 nm as the excitation source with a spectral resolution of 2 cm^{-1}. The beam was focused on the sample with a 100 × objective and the laser power reduced to 0.4 mW (5%) by means of optical filters. Spectra were obtained in the 500–1950 cm^{-1} range with 60 s exposure and as the average of multiple acquisitions.

Temperature Programmed Reduction of H_2 (H_2-TPR) was performed in a tubular vertical furnace with 50 mg of the catalysts in a flow of 10 vol% H_2/Ar (30 cm^3_{STP} min^{-1}) from room temperature to 900 °C with a heating rate of 5 °C min^{-1}. The H_2 consumption was monitored by a mass spectrometer (Pfeiffer Omnistar GSD-301).

The number of active metal on the surface of the Co-containing carbon fibers catalysts was measured by flowing H_2-chemisorption technique, similar to that reported by Bartholomew et al. [49]. The catalysts (0.2 g) were reduced in situ under flowing H_2 (50 cm^3_{STP} min^{-1}, 99.95%) at 350 °C for 3 h and at a heating rate of 2 °C min^{-1} in order to reproduce conditions used in the reduction stage prior to FTS reaction. After reduction, catalysts were cooled to 0 ± 3 ºC in flowing hydrogen at 1.5 °C min^{-1} (during this process, the H_2 adsorption on the catalyst takes place). Afterwards, the H_2 flow was changed to argon flow (40 cm^3_{STP} min^{-1}, 99.998%) and maintained for 1 h at that temperature in order to purge the gaseous phase and remove physisorbed hydrogen from the catalyst cell and ensure full monolayer coverage of chemisorbed hydrogen. The samples were then heated (at a heating rate of 20 °C min^{-1}) up to the reduction temperature. The H_2-uptake was calculated by integration of the area under the MS signal. Fig. S1 shows the H_2-MS responses for the catalysts during the TPD. Particle size estimations were based on cobalt particles with spherical geometry, assuming complete reduction of the metal and an H/Co adsorption stoichiometry of 1, using the formula $d(Co)_H = 96.2/\%D$, where $d(Co)_H$ is the cobalt particle diameter (nm) and %D the percentage of dispersion. Here, %D = 1.179X/W, where W is the weight percentage of cobalt (as measured by ICP-OES) and X is the total H_2 uptake, in micromoles per gram of catalyst.

SEM and TEM images were obtained using a JSM-6490LV (JEOL) microscope operated at 25 kV voltage and a Talos F200X (FEI) transmission electron microscope at an accelerating voltage of 200 kV, respectively. To determine the dispersion of elements present in the catalysts, energy dispersive X-ray (EDX) elemental mapping was also analyzed. Cobalt particle size distributions were determined upon counting between 100 and 200 particles on each sample.

2.3. Fischer-Tropsch Synthesis

The FTS reaction was performed in a six-flow fixed-bed microreactor setup previously described elsewhere [50]. Typically, 0.40 g of catalyst was reduced in-situ by 80 cm^3_{STP} min^{-1} of H_2 at 350 °C for 3 h at atmospheric pressure followed by cooling down to 180 °C. After increasing pressure to 20 bar, a flow of CO was gradually introduced to the reactor at 180 ºC in order to reach an H_2/CO molar ratio of 1 or 2 and different space velocities of 3.3, 4, 5.3 and 8 m^3_{STP} Kg_{cat}^{-1} h^{-1}. Finally, the reactor temperature was heated to the reaction temperature (220 and 240 °C) and FTS runs were performed for 70 h. A rate of 2 °C min^{-1} was applied for all the heating steps. Permanent gases as well as light hydrocarbons in the gas phase were analyzed online by a Compact GC (*Interscience*) equipped with three columns and detectors in parallel, using He as carrier gas. In the first column (Carboxen 1010, 10 m × 0.32 mm) N_2, CO, CH_4 and CO_2 were separated at 60 °C and detected by a TCD. In the second column (Al_2O_3/KCl, 10 m × 0.32 mm) and FID detection, separation between all C1–C4 components was achieved at 160 °C. In the third column (RTx-1 0.5 μm, 15 m × 0.32 mm) C5–C10 hydrocarbons were separated at 80 °C and analyzed by FID.

During the experiment, heavy hydrocarbons (waxes) were collected by gas/liquid separators at 175 °C and reaction pressure. Once expanded to atmospheric pressure the lighter hydrocarbons and water were collected in cold traps at ca. 5 °C. After separation from water, these liquid hydrocarbons as well as the waxes were weighted, dissolved in CS_2 and analyzed offline by a simulated distillation (SimDis) GC (Hewlett Packard 5890, Series II) equipped with an FID and HP-1 column (7.5 m × 0.53 mm, Film Thickness 2.65 μm), using He as carrier gas. During the analysis, the oven temperature was ramped from 35 to 350 ºC (15 °C min^{-1}) and kept at the final temperature for 5 min

Eqs. (1) and (2) define CO conversion and carbon selectivity, respectively, where X_{CO} stands for CO conversion, $F_{in,CO}$ and $F_{out,CO}$ indicates the molar flows of CO at the reactor inlet and outlet, respectively, F_{Cn} is the total molar flow of hydrocarbons with n carbon number, F_{CO2} is the molar flow of CO_2 at the reactor outlet and S_{C_n} is the carbon selectivity towards a product with n carbon atoms. The carbon selectivity was determined after 70 h time-on stream (TOS). The catalytic activity is also expressed in terms of cobalt-time-yield (CTY) (Eq. (3)), defined as moles of CO converted per gram of Co per second.

$$X_{CO} = \frac{F_{in,CO} - F_{out,CO}}{F_{in,CO}} \times 100, \quad (1)$$

$$S_{Cn} = \frac{nF_{Cn}}{F_{CO_2} + \sum_{n=1}^{N} nF_{Cn}} \times 100, \quad (2)$$

$$CTY = \frac{X_{CO}F_{in,CO}}{m_{Co}} \quad (3)$$

The chain growth probability α is defined in terms of the rate of polymerization (r_p) and the rate of termination (r_t) of the growing hydrocarbons, according to Eq. (4). Eq. (5) represents the Anderson-Schulz Flory (ASF) hydrocarbon product distribution in terms of molar fractions. The α value has been calculated from the slope of ln (y_{Cn}) as a function of n, the hydrocarbon chain length.

$$\alpha = \frac{r_p}{r_p + r_t}, \quad (4)$$

$$y_{Cn} = (1-\alpha)\,\alpha^{n-1} \quad (5)$$

3. Results and discussion

3.1. Cobalt-containing carbon fibers catalysts preparation

Lignin fibers and cobalt-containing lignin fibers were synthesized by co-axial electrospinning of Alcell lignin and cobalt-lignin spinnable solutions according to the synthetic procedure described in Scheme 1. Prior to the heat treatment process to produce carbon fibers, a thermostabilization stage was required due to the low glass transition temperature (T_g) of lignin, quite below the heat treatment temperature [51]. Therefore, an air oxidation process was performed at a very low heating rate for the thermo-oxidative stabilization to ensure an increase of the T_g via oxygen cross-linking reactions that incorporate oxygen groups into the structure of the nanofibers, and thus avoiding fibers softening an melting during the heat treatment stage [37].

After the air stabilization process, the surface oxygen content (calculated from XPS) increased from 26.6 to 32.6% for SLF and from 28.1 to 30.4% and from 27.3 to 31.8% for SCo@LF and SCo/LF, respectively. The relatively higher amount of surface oxygen observed for SCo/LF compared to SCo@LF was probably attributed to the higher percentage of metal on its surface.

The heat treatment process conditions such as heating rate, temperature and holding time are key parameters to control the porosity, Co

NPs size and chemical phase of the resulting Co-containing carbon fibers. Therefore, the study of their thermal decomposition behavior under nitrogen was of primary importance before conversion of the stabilized lignin fibers into carbon fibers. The thermogravimetric curves in N_2 and the evolution of volatile gases for the thermal stabilized samples, SLF and SCo@LF, during heating up to 900 ºC are presented in Fig. 1a and b, respectively, whereas Table S1 summarizes the total amounts of H_2O, CO, CO_2, CH_4 and H_2 desorbed from the samples, obtained by integration of the areas under the MS peak. These results suggest that the main weight-loss for SLF takes place within a relatively narrow temperature range (from 360 to 650 ˚C (Fig. 1a)), whereas this temperature range was considerable increased for SCo@LF (from 240 to 850 ˚C (Fig. 1b)). A relatively large amount of H_2O, CO and CO_2 is formed from both samples due to the decomposition of the high volatile matter content (c.a. 60% for Alcell Lignin [32]) and to oxidation reactions, which may take place with the oxygen retained by the lignin fibers during the stabilization process, resulting in a total oxygen evolved of 24.4 and 32.2 *wt.* % for SLF and SCo@LF, respectively (Table S1). The H_2O evolution occurs over a wide temperature range for the stabilized lignin fibers (SLF) decomposition, with a main broad peak observed at 425 ºC and two shoulders at around 220 and 650 ºC (see Fig. 1c). The decomposition of polymeric constituents by dehydration of neighbor carboxylic groups, with the formation of anhydride type groups, and of phenolic hydroxyl and/or hydroquinone groups of the stabilized lignin fiber matrix could be responsible for the observed presence of water [52]. The decomposition of these groups of the stabilized lignin fibers matrix could also account for the evolution of CO_2 at similar temperatures [39,53]. The broad curve observed for CO at higher temperatures, with a maximum at 525 ºC, can be attributed to the cracking of carbonyl (C-O-C) and carboxyl (C═O) groups of the lignin fiber matrix and to other carbon fiber formation reactions [52,53]. There is also a noticeable evolution of H_2 above 600 ˚C probably associated to the depolymerization of the abundant phenyl groups of the lignin fibers and to condensation reaction of the carbonaceous structure formed during the heat treatment at high temperature, although the thermal cracking of hydrocarbons produced by decomposition of lignin during heat treatment cannot be ruled out [53]. The presence of the cobalt salt in the lignin solution to produce the Co-containing stabilized lignin fibers (SCo@LF) seems to favor an increase of the amount of water, CO_2, CO and H_2 evolved during the heat treatment (see Fig. 1d), not only due to the presence of oxygen and water in the salt, but to the possibility that cobalt may favor further oxidation of the lignin fibers matrix during the stabilization process. As already indicated, the evolution of CO_2 (and CO) could be also attributed to a self-induced carbon oxidation by the retained oxygen during the stabilization process, which may be catalyzed by the presence of cobalt in SCo@LF. The curve for the release of H_2 (and CO) from SCo@LF shows two sharp peaks at 500 and 830 ˚C (not observed for those of SLF), which coincide with the temperature for the reduction steps of CoO(OH) to Co_3O_4 and from this further to CoO [54]. In addition to this, the reduction of CoO to metallic cobalt by the carbon fiber and/or by the likely hydrocarbons (tars) formed during the thermal treatment of lignin should not be neglected [55]. Interestingly, the significant increase of H_2 evolved from SCo@LF from 500 ˚C is accompanied by a fast decrease of the amount of H_2O released (and in a lesser extent of CO_2) from this sample during the thermal treatment, suggesting that the evolution of water (and CO_2) may contribute to a partial gasification of the formed carbon fiber catalyzed by the cobalt oxides (and/or metallic Co) centers [56]. The steam reforming of condensed carbon structures (tars) formed from the pyrolysis of the lignin fibers cannot be rule out, which may be also catalyzed by the high presence of reduced cobalt in the surface of the lignin-derived carbon fibers formed during the heat treatment, a well-known catalyst for this process [57]. On the other hand, the evolution of CH_4 takes place at low temperatures (< 500 ˚C), probably as a consequence of the breakdown

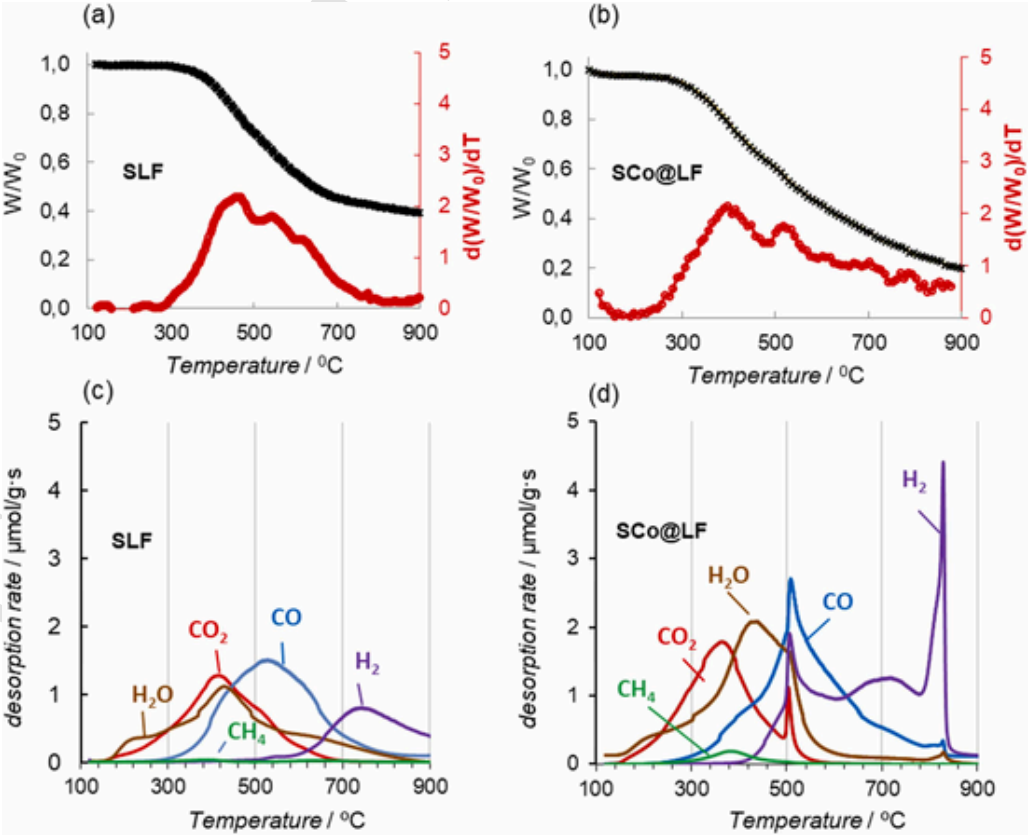

Fig. 1. Thermogravimetric analysis (a,b) and amount of CO, CO_2, CH_4, H_2O and H_2 evolved (c,d) from SLF (a, c) and SCo@LF (b,d) during heat treatment in N_2 atmosphere (5 ˚C min^{-1}).

of methoxy groups (-O-CH_3), typical in lignin decomposition reaction [53].

Table 1 presents the yields of the lignin-derived fiber and cobalt-containing fibers stabilization and heat treatment processes. The stabilization yields take into account not only the weight loss associated to condensation and decarboxylation reactions of the lignin fibers, but also the fibers surface oxidation producing carbonyl, carboxyl, anhydride and ester type surface groups, which may evolved as H_2O, CO and CO_2 during the subsequent heat treatment stage (Fig. 1). The stabilization yields of the as-spun Co-containing lignin fibers were higher than that of the pure as-spun lignin fibers. This fact may be attributed to the lower heating rate used for SLF during the stabilization stage (12.5 fold lower than SCo@LF) and longer holding time at 200 ºC (100 h instead of 1 for SCo@LF) that may have produced a higher decomposition of lignin during this long process. Another reason is the higher oxidation degree of cobalt-containing lignin fibers, with the corresponding mass gain, as derived from the larger oxygen content observed for this sample (Table S1). The presence of Co reduced considerably the time needed to stabilize the lignin fiber, avoiding fiber melting during the subsequent heat treatment, probably due to a favorable lignin surface oxidation conducted through cross-linked reactions catalyzed by cobalt oxides. Thus, the stabilization of Co-containing lignin fibers was carried out at faster heating rate and with a less holding time at the final stabilization temperature than those for the as-spun pure lignin fiber, which will be evidenced from SEM images in the next section. Similar results were observed when phosphoric acid was added to the lignin solutions, generating phosphate (and/or polyphosphate) esters in the lignin fiber structure that allowed to stabilize lignin fibers 35 times faster than bare lignin fibers [37]. Furthermore, it must be pointed out that the heat treatment yields obtained for Co@LF corresponds quite well with the predicted values from the thermogravimetric analysis. The yield of this treatment, defined as the weight of the heat-treated sample to the stabilized material, on a dry basis, decreases with the pyrolysis temperature, indicating a deeper devolatilization of the carbonaceous matrix with temperature. These yields are, moreover, lower than that for pure lignin-derived CF (without cobalt) heat treated at 500 ºC (Table 1), or prepared at a higher heat treatment temperature range (600–800 ˚C), as reported in a previous work [39]. Furthermore, the lower heat treatment yield observed when cobalt is present in the carbon precursor fibers may be due to the carbon fibers self-induced oxidation and gasification during the carbonization stage as confirmed from the results reported in Fig. 1, which is also in concordance with previous results reported by our research group based on the preparation of Pt-containing carbon fibers [38]. Here, an increase in the amount of Pt on the preparation of Pt-containing carbon fibers resulted in a lower carbon yield during the heat treatment stage.

Taking into account the results obtained from the TG analysis and its unsteady nature, the temperature and time for the heat treatment of Co-containing stabilized fibers were set at 500, 650 and 800 ˚C for 1 h. In addition to this, a heating rate of 2 ˚C min^{-1} was selected to avoid the formation of a wide size distribution of Co nanoparticles (NPs) over the carbon matrix, given the potential diffusional effect of the released reducing gases on the growth of Co NPs [23]. The pure and Co-containing carbon fibers samples were characterized with different experimental techniques and their physicochemical properties are discussed in the following section.

Table 1
Yields of the stabilization step and heat treatment process at different temperatures for several lignin-derived fibers.

	Yields / *wt.* %		
Sample	Stabilization	Heat treatment	Overall
CF-500	76.0	54.5	41.4
Co/CF-500	81.4	50.7	41.3
Co@CF-500	82.7	48.6	40.2
Co@CF-650	82.7	39.8	32.9
Co@CF-800	82.7	27.0	20.6

3.2. Co-containing carbon fibers catalysts characterization

Fig. 2a shows SEM micrographs of the as-spun lignin fibers containing cobalt on the overall carbon fiber structure, whereas Fig. 2b and c show images of the same material before and after the heat treatment stage performed at 500 ˚C, respectively. A fiber morphology and non-interconnected fibers were clearly observed before and after the heat treatment stage. These results confirm that the oxidative thermostabilization treatment applied to the as-spun material avoid fiber fusion, without significant modification of the fiber size, despite the relatively higher stabilization heating rate (1 ºC/min) and shorter holding

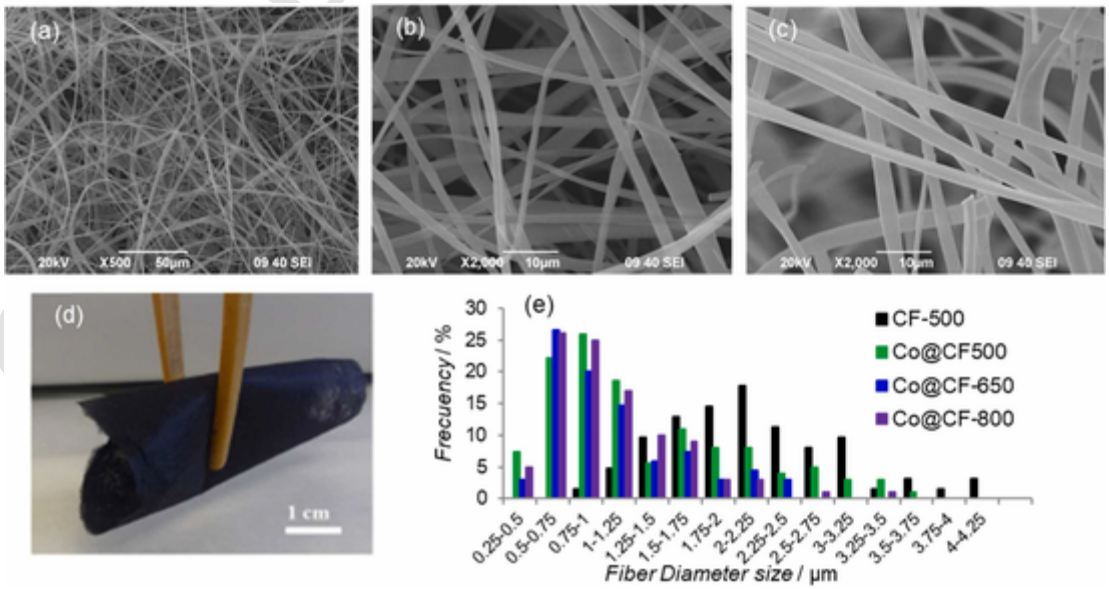

Fig. 2. SEM images of as-spun Co-containing lignin fibers (Co@LF) (a) stabilized Co-containing lignin fibers (SCo@LF) (b) and stabilized Co-containing lignin fibers heat treated at 500 ºC (Co@CF-500) (c), photo of Co@CF-500 showing the flexibility of the fibrillar catalyst (d) and histogram of fiber diameters from the results of SEM for CF-500 and Co@CF-500, – 650 and – 800 (e).

time (1 h) used for the case of lignin fibers that contain Co compared to the low stabilization heating rate and longer holding time needed for the as-spun pure lignin fibers (0.08 °C min^{-1} and 100 h) [37,39]. In addition, the image shown in Fig. 2d of Co@CF-500 clearly evidences the good flexibility of this type of carbon fibers to be adapted as a catalytic-bed to a tubular plug flow reactor. The fiber diameter size distribution obtained for CF-500 by this preparation method presented a wide diameter size range, between 1.0 and 4 μm, whereas fiber sizes from 0.25 μm and 2.0 μm were observed when cobalt is added to the spinnable solution and the lignin fibers were stabilized and heat treated at similar conditions, Co@CF-500. The addition of salts and other conductive polymers that increase the solution conductivity to be spun have been reported to reduce fiber size [58]. In addition, Co@CF fibers size diameters slightly decreased with increasing heat treatment temperature from 500 to 800 °C, probably associated to the shrinkage of the carbon material with heat treatment temperature.

Fig. 3a presents the N_2 adsorption-desorption isotherms for CF-500 and Co-containing carbon fibers catalysts heat treated at different temperatures, whereas Table 2 reports the values of the textural parameters derived from N_2 and CO_2 adsorption isotherms. The isotherm of CF-500 is of type I and exhibits a sharp nitrogen uptake increase at very low relative pressures and an almost horizontal plateau at higher relative pressures, indicating that the porous texture consists predominantly of very narrow micropores. In contrast, the presence of cobalt in the process of producing the carbon fibers generated fibrillar carbon materials with greater development of wider microporosity and of the mesoporosity with increasing heat treatment temperature, as indicated for an increase in the amount of N_2 adsorbed at low and medium relative pressure values and a larger hysteresis loop, essentially due to the self-induced carbon gasification during the heat treatment process. As it can be seen in Table 2, V_{DR} values obtained from the CO_2 adsorption isotherms were always higher than those obtained from the N_2 adsorption data, which indicates the presence of narrow micropores with pore sizes lower than 0.7 nm [59]. As it was mentioned, an increase in the heat treatment temperature from 500 to 800 ºC also produced an increase of the N_2 adsorbed at higher relative pressures, with larger hysteresis loop at high relative pressures, indicating a widening of the porous texture as a consequence of a greater extent of volatile matter released and to the favored carbon gasification with temperature. H4 hysteresis loop that closes at $P/P_0 = 0.4$ is observed for Co@CF samples, typical of materials with narrow slit-like mesopores, and the type I isotherm character is indicative of microporosity [60]. However, a H2 type hysteresis loop can be observed at medium/high relative pressures for Co/CF-500, often associated to pores with narrow necks and wide bodies [60]. The mesopore surface area of Co@CF increases from 60 to 112 m^2g^{-1} after the heat treatment at 500 and 800 ºC, respectively, and the mesopore volume increases, as well, from 0.055 to 0.243 cm^3g^{-1}. Alongside, the micropore volume increases from 0.144 to 0.173 cm^3g^{-1}. DFT pore size distribution (Fig. 3b) clearly confirms the development of the micro- and mesoporosity of the carbon fibers with the presence of cobalt. The mean micropore size is 10.6 Å for Co@CF-500, which is slightly higher than that calculated for the bare carbon fiber, CF-500 (8.7 Å). In contrast, it is observed a shift of the mean micropore size distribution to slightly lower values upon increasing the heat treatment temperature, from 10.6 Å at 500 ºC to 6.1 Å at 800 ºC. This is probably caused by the shrinkage of the carbon fiber porous structure with temperature as also revealed the histogram of fiber diameters (Fig. 2e). It has to be noted that at this high heat treatment temperature, the catalyst (Co@CF-800) also revealed an incipient formation of narrower micropores, of about 1.2 Å and a higher development of mesoporosity (Fig. 3b insert), with mean mesopores size of about 30.8 Å, which is slightly lower than those obtained for Co/CF-500 (70.2 Å) and Co@CF-650 (33.0 Å). As aforementioned, this is caused by the higher devolatilization and self-gasification of the Co-containing carbon fibers at higher heat treatment temperatures (Fig. 1 and Table S1). For heterogeneous catalytic applications, a wider micro- and mesoporosity in the carbon support can facilitate the diffusion of the reactants and liquid products and thus enhance the CO conversion and C5+ selectivity of the catalyst for FTS, as reported in an earlier study [24].

XPS characterization was further conducted for all Co-containing CFs to analyze the surface element composition as well as the chemical states of the surface cobalt species. Co_{2p}, O_{1s}, C_{1s} and N_{1s} were detected from the XPS full spectra of the catalysts at 780.3, 532.9, 284.5 and 399.5 eV, respectively [20,24]. The XPS spectra of Co_{2p} for the Co-containing carbon fiber catalysts are shown in Fig. 4, whereas the mass surface and bulk concentrations of the heat treated fibers (without and with cobalt) obtained from XPS and ICP-OES analysis, respectively, are reported in Table 3. Carbon and oxygen were the main elements found on the surface of the Co-containing carbon fibers catalysts, with lower amount of cobalt. Nitrogen was also detected at very low concentration (0.2–0.7%), probably being a remnant of nitrogen originally present in the Alcell lignin used as carbon precursor. Some reports have shown that nitrogen species in Co-containing carbon catalysts and in higher concentrations (2–22 *wt.* %) might act as efficient electron donors, influencing the CO adsorption-dissociation process and promoting the synthesis of short-chain hydrocarbons in the FTS [23,24,61]. As expected, the amount of surface oxygen decreased from 16.0 to 4.5 *wt.*% as the heat treatment temperature increased from 500 to 800 ºC, respectively, and the carbon surface content increased (from 81.5 *wt.*% at 500 ºC to 92.8 *wt.*% at 800 ºC), due to the removal of oxygen as H_2O, CO and CO_2 (Fig. 1b and Table S1). On the other hand, the data related to the cobalt mass surface concentration, obtained from XPS, and the bulk Co concentration (measured by ICP-OES) pointed out that around 69% of

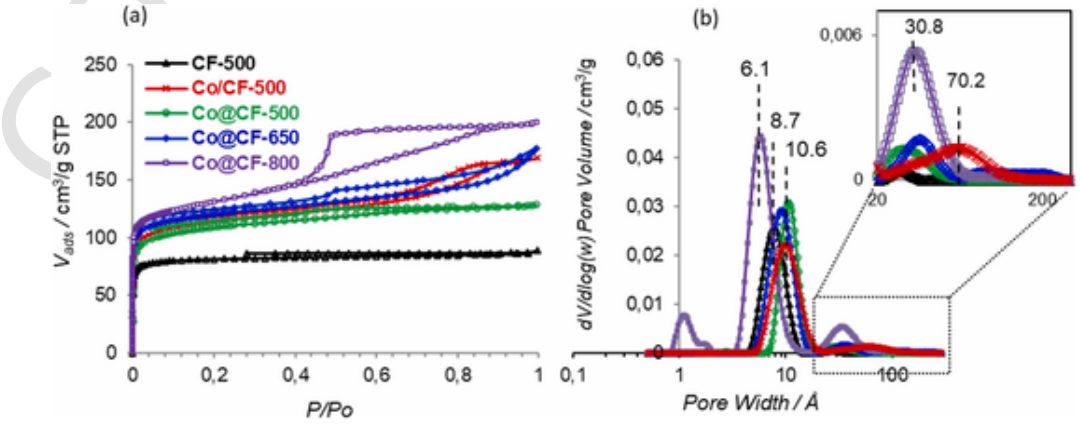

Fig. 3. Nitrogen adsorption–desorption isotherms at 77 K (a) and DFT pore size distributions of the CFs with and without cobalt (b).

Table 2
Textural properties of the lignin-derived CFs heat treated at 500 ºC and the different lignin-derived Co-containing CF catalysts.

Sample	N_2 isotherm					CO_2 isotherm	
	S/ $m^2\ g^{-1}$		V / $cm^3\ g^{-1}$			S_{DR}[a] / $m^2\ g^{-1}$	V_{DR}[a] / $cm^3\ g^{-1}$
	S_{BET}[b]	S_{meso}[c]	V_{total}	V_{micro}[d]	V_{meso}[e]		
CF-500	326	11	0.140	0.120	0.010	505	0.200
Co/CF-500	418	71	0.262	0.148	0.114	428	0.170
Co@CF-500	400	60	0.199	0.144	0.055	434	0.174
Co@CF-650	438	68	0.248	0.160	0.116	492	0.197
Co@CF-800	460	112	0.276	0.173	0.243	510	0.184

[a] Micropore volume and surface area obtained by the Dubinin–Radushkevich (DR) method applied to the CO_2 isotherm.
[b] BET surface area.
[c] Mesopore surface area obtained from the t-plot applied to the N_2 isotherm.
[d] Micropore volume obtained from the t-plot.
[e] Mesopore volume calculated as $V_{meso} = V_{total}\ (P/P_0 = 0.95) - V_{micro}$.

the Co was mainly located on the surface of Co/CF-500 catalyst, whereas only 27% of cobalt were located on the surface of Co@CF-500, – 650 catalysts and 21% for Co@ 800 sample. Moreover, the amount of bulk cobalt gradually increases with the carbonization temperature due to the decrease of the overall carbon yield (Table 1) and the results were very close to the value calculated from the cobalt intake.

Fig. 4 shows the deconvolution of the Co_{2p} spectra of the Co-containing carbon fibers catalysts. The Co_{2p} spectra displays the characteristic doublet corresponding to the spin-orbit coupling ($2p_{3/2}$, $2p_{1/2}$) with an area ratio of 0.5 and a distance between peaks of 15 eV, accompanied by a satellite peak with a binding energy of about 6 eV higher than that of the Co_{2p} peak [62]. The component at a binding energy of about 780.5 eV is attributed to the presence of Co(II)/Co(III) phases as in the Co_3O_4 spinnel and the shake-up satellite peak is related to the presence of Co^{2+} ions in an octahedral symmetry, typical of CoO [63]. Deconvolution of the Co_{2p} spectra for all the catalysts showed that both Co(II) and Co(III) species were present on the surface of the catalysts. However, at high pyrolysis temperature the fraction of Co(II) and metallic cobalt increased. The peak related to Co_3O_4 component observed at a higher binding energy was more intense compared to the shake-up satellite peak for the catalysts pyrolyzed at 500 ºC, Co@CF-500 (Fig. 4a) and Co/CF-500 (Fig. 4b), indicating that Co_3O_4 was the dominant cobalt phase on these two samples. However, Co(II) and metallic cobalt species were gradually formed on the surface of the carbon fiber catalysts at higher pyrolysis temperatures (> 500 ˚C), probably caused by an in-situ catalyst reduction favored by the released reducing gases (e.g. H_2 and CO) generated during the carbonization of lignin and by the carbon fiber itself [55]. These results confirmed the incipient reduction of cobalt oxide above a pyrolysis temperature of 500 °C and the role of cobalt active sites to catalyze the gasification reactions during the carbonization of lignin, as aforementioned from the results obtained by TG-MS showed in Fig. 1d.

In this sense, it is likely that the carbonization of lignin fibers, the releasing of hydrocarbons or tars and the reduction of Co cations are expected to occur simultaneously, leading to entrapped metallic Co particles in the carbonaceous matrix. Nevertheless, the partial steam gasification of the Co-containing lignin carbon fibers (Fig. 1d) during the heat treatment at high temperature may favor the mobility and thus sintering of Co nanoparticles, which would explain the low surface cobalt content (measured by XPS, Table 3), specially at high heat treatment temperatures. For instance, the surface cobalt content for Co@CF-800 is only 2.5 *wt.* %, relatively much lower than the bulk cobalt content measured by ICP-OES (12.1 wt%). On the other hand, metallic cobalt has been reported to catalyzed the graphitization of the carbonaceous substrates, preferentially in the interphase cobalt/carbon during the thermal treatment [23,64]. The possible graphitization of the carbon matrix surrounding the cobalt NPs could have prevented this Co

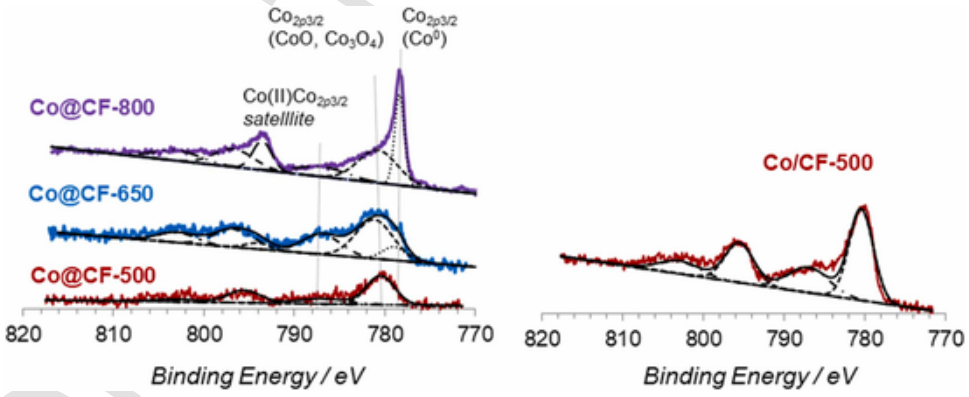

Fig. 4. XPS spectra (Co_{2p} region) of the different Co-containing CFs catalysts.

Table 3
Mass surface concentrations (%) obtained by XPS, cobalt content from ICP-OES, cobalt particle size from XRD and TEM, H_2 uptake and calculated cobalt dispersion and cobalt particle size from H_2-Chemisorption for the Co-containing CF catalysts.

Sample	XPS, wt%				ICP-OES wt%	XRD		TEM	H_2-Chemisorption		
	C_{1s}	O_{1s}	Co_{2p}	N_{1s}	Co	d $(Co_3O_4)_{XRD}$ / nm	d $(Co)_{XRD}$ / nm	d $(Co)_T$	H_2 uptake / μmol/g	D[a] / %	d $(Co)_H$ /nm
CF-500	84.1	15.4	0.00	0.50	n.a.[b]	n.a.	n.a.	n.a.	n.a.	n.a.	n.a.
Co/CF-500	83.6	13.0	2.7	0.7	3.9	9.3	14.2	15.9	17.8	5.4	17.7
Co@CF-500	81.5	16.0	1.9	0.6	7.2	7.8	n.d.[c]	6.8	58.4	9.9	9.7
Co@CF-650	88.9	8.4	2.1	0.6	8.0	n.d.	13.6	14.6	44.4	6.5	14.7
Co@CF-800	92.8	4.5	2.5	0.2	12.1	n.d.	29.5	32.4	22.8	2.6	38.0

[a] Calculation based on HCo = 1.
[b] n.a.: not applicable.
[c] n.d.: not determined.

species from sintering with the heat treatment to a greater extent and from air oxidation too, once the samples were exposed to atmospheric air during passivation or storage period before their characterization. For this reason, metallic cobalt was detected on the surface of Co@CF-650 and Co@CF-800 samples (Fig. 4). Similar results have been reported for Co^0 crystallites obtained from carbonization of Co-derived MOFs [23–25,64].

The XRD patterns of the Co-containing carbon catalysts prepared in this work are shown in Fig. 5. Co@CF-500 exhibits only a small and broad diffraction peak at 2θ = 43 º resulting from the presence of Co_3O_4 crystal phase, as reported for cobalt supported on activated carbons and carbon nanotubes [12,19,65]. The absent of clearly defined diffraction XRD patterns for this sample suggests a high dispersion of cobalt species. At higher heat treatment temperature, diffraction XRD patterns of metallic cobalt (2θ = 51.8°, 60.6°) with a face-centered cubic (fcc) crystal structure (PDF No. 15–0806) and graphite (2θ = 19°, 30.6°) are gradually observed (for samples heat treated at 650 and 800 °C, respectively), whereas that of Co_3O_4 almost disappear at a heating temperature of 800 °C, indicating that cobalt oxide is being reduced during the heat treatment step, in line with the conclusions from XPS results (Fig. 4a). Furthermore, at higher heating temperature the metallic cobalt peak become narrower and sharper, indicating larger crystallite size of cobalt NPs. The average crystallite sizes of Co_3O_4 and Co were determined by applying the Debye–Scherrer equation to the most intense diffraction peaks (2θ = 43° and 51.8°, respectively) and the results are showed in Table 3. The average crystallite sizes of the samples prepared at different pyrolysis temperatures (Co@CF-500, 650, 800) show a clear dependence on the pyrolysis temperature, with larger particles being formed in the samples treated at higher temperatures. A mixture of Co_3O_4 and metallic cobalt characterizes the XRD profile of Co/CF-500 sample, where most of the cobalt is mainly deposited on the external carbon surface according to the XPS results. The most intense peak associated to metallic cobalt suggested that larger cobalt crystallite sizes were formed on the surface of Co/CF-500 compared to those of Co@CF-500, in which cobalt is deposited on the whole carbon fiber. This fact points out the confinement effect of the carbonaceous matrix to allow a high dispersion of Co species in Co@CF-type samples, without a significant sintering in the lignin-derived carbon fiber matrix. The effect on the size of the Co NPs has been also analysed from TEM analysis.

Figs. 6 and S3 shows TEM images and EDX elemental maps of the Co-containing carbon fibers, respectively. As shown, Co@CF-500 reveals cobalt NPs homogeneously dispersed overall the fiber structure and uniform NPs sizes in all the fiber both at medium and high-resolution TEM images (Fig. 6a and b). The EDX elemental maps also evidence the high dispersion of Co on the carbon fiber (Fig. S3a). Clearly, higher pyrolysis temperatures induce aggregation of Co to larger NPs size, as revealed from TEM images in Fig. 6d and g. This was more clearly reflected from the corresponding particle size distribution histograms. The sample heat treated at 500 °C (Co@CF-500) presents a narrow cobalt particle size distribution with overage particles size between 9 and 11 nm. Similarly, the Co particles on Co@CF-650 are fairly uniform, with the most abundant ones around 10–13 nm in size, in agreement with the XRD results. However, the width of the PSD increased considerable at °800C. Furthermore, the high-resolution (HR)-TEM image of Co@CF-800, presented in Fig. 6h, shows that the cobalt phase is embedded in the carbon matrix and encapsulated by a few nanolayers of graphitic-type carbon shell, inferring a highly stable catalytic system. Contrary to this, Co/CF-500 shows a wider particle size distribution than Co@CF-500 with Co NPs ranging between 13 and 18 nm (Fig. 6l). The results in Fig. 6k and the EDX mapping distribution of Co, showed in Fig. S4, revealed that the cobalt NPs are located mostly on the outermost external surface. These results suggested that in Co@CF type catalysts the carbon material surrounding the cobalt NPs seemed to act as a protective layer, preventing the particles from sintering at high pyrolysis temperatures. The average cobalt particle size for each catalyst obtained from TEM ($d(Co)_T$) is summarized in Table 3. Similar results have been observed by other authors studying the pyrolysis of ZIF-8 MOF (containing Co), in which the cobalt NPs are also encapsulated in a carbonaceous carbon matrix upon a thermal treatment in inert conditions at high temperatures [23,64]. Nevertheless, in the present work, Co sintering might have been also favored by the self-induced oxidation and gasification of the carbonaceous fiber matrix, particularly at higher heat treatment temperature, due to the higher Co NPs sizes detected within the same heating temperature range studied.

The hydrogen uptake data, the calculated apparent dispersions and metallic cobalt particle size of the catalysts are presented in Table 3. It was not possible to obtain the degree of reduction of cobalt by oxygen titration, due to the interference of oxygen with the carbon support, in line with other works for cobalt supported on carbon-based materials [16,23]. Therefore, complete cobalt reduction for the Co-containing samples has been assumed. In fact, metallic cobalt was already detected on the surface of the samples according to XPS and XRD before the reduction process in H_2 (Figs. 4 and 5), due to the heat treatment of the Co-containing lignin fibers, as it was already discussed from results reported in Fig. 1. It is observed that the metallic cobalt dispersion is gradually decreased from 9.6% to 2.6% and the metallic cobalt particle size increased from 9.7 nm to 38.0 nm when the heat-treatment temperature is increased from 500 to 800 °C, respectively. The results for the metallic cobalt particle size over the different Co-containing carbon fibers catalysts are well consistent for most catalysts when the values determined by XRD ($d(Co)_{XRD}$), H_2-chemisorption ($d(Co)_H$) and TEM ($d(Co)_T$) are compared. However, in the case of Co@CF-800, the catalyst prepared at the highest heat-treatment temperature, the value for $d(Co)_H$ is relatively higher than those for $d(Co)_T$ and $d(Co)_{XRD}$, which may be associated to the presence of unreduced cobalt oxides and/or the presence of inaccessible metallic cobalt sites, leading to a lower amount of chemisorbed H_2 and an increased in metallic cobalt particle size error [16,66].

Regarding the structural nature of carbon in the Co-containing carbon fibers, a few nanolayers of graphitic-type carbon shell were observed for the representative HRTEM images of Co@CF-800 (Fig. 6k). In order to further investigate the formation of graphitic carbon and to probe its extent of graphitization, the catalysts were characterized by Raman spectroscopy and the results are shown in Fig. 7a. The first-order Raman spectral region of the Co-containing carbon fibers clearly reveal the characteristic overlapping bands of carbon, at about 1580 and 1360 cm^{-1}, which are associated to the graphitic lattice vibration mode with E2g symmetry (G band) and disordered or defect carbon (D band), respectively [67,68]. In addition to this, the spectra reveal the presence of other bands at 1480 and 1180 cm^{-1}, which are attribute to oxygen functional groups and/or to impurity ions, i.e., cobalt, respec-

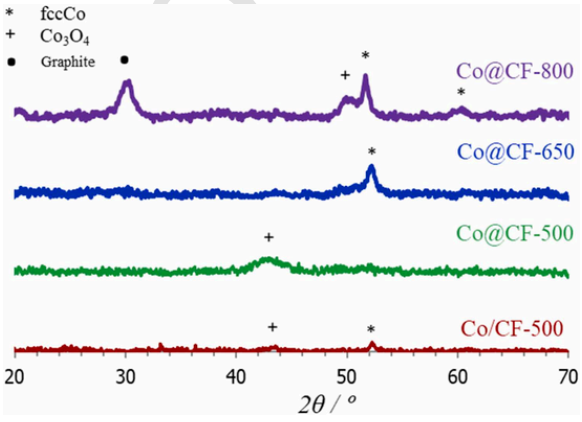

Fig. 5. X-ray diffraction patterns of the Co-containing carbon fiber catalysts.

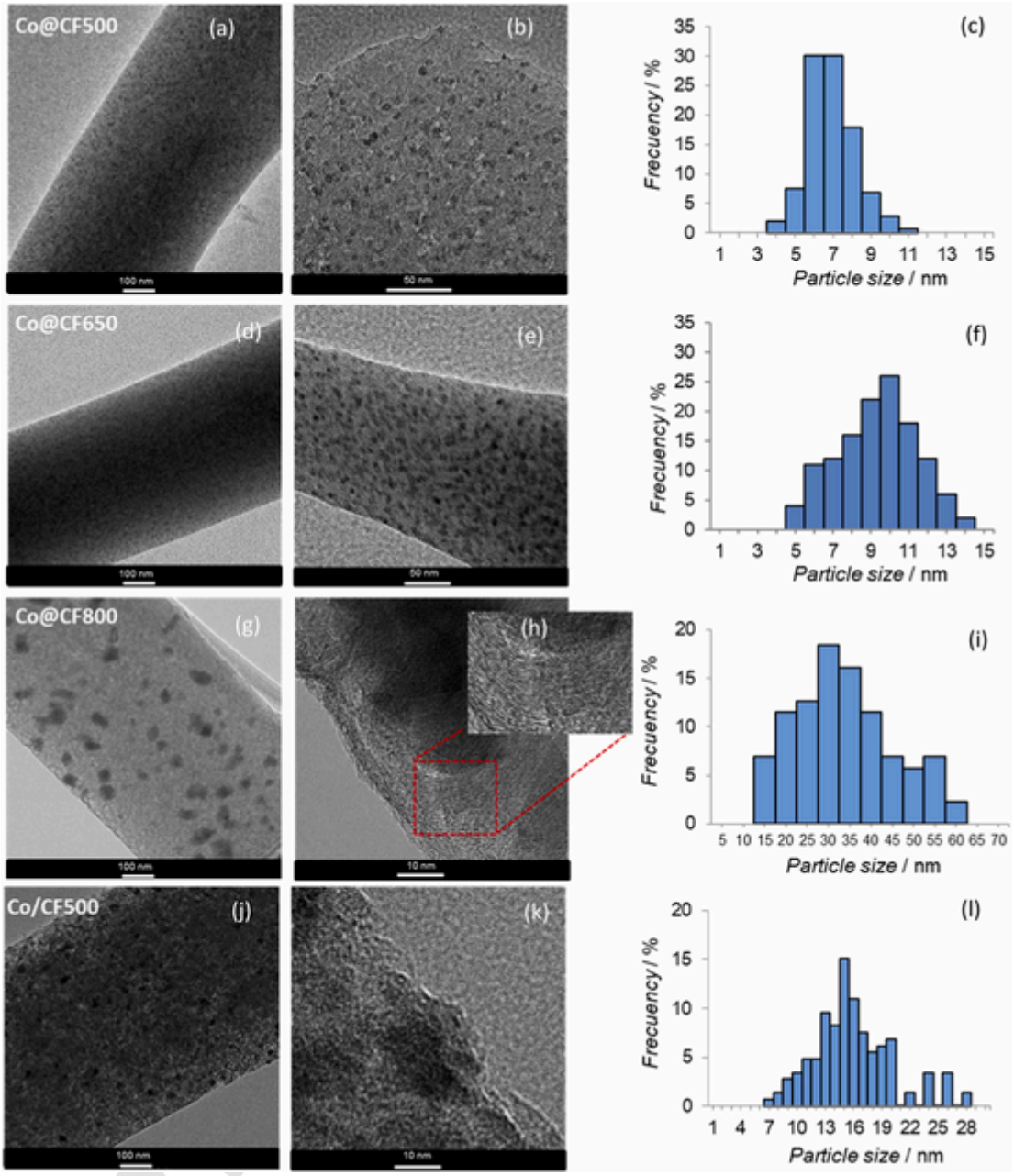

Fig. 6. TEM images and PSD of Co@CF-500 (a, b, c), Co@CF-650 (d, e, f), Co@CF- 800 (g, h, i) and Co/CF-500 (j, k, l).

tively. Fig. 7b shows the deconvolution of the Raman spectrum for Co@CF-650 [39,68] and the spectral parameters (Raman shift (ν_D and ν_G), full widths at half maximum (FWHM) of D and G bands and intensity (peak area ratios) are reported in Table S2. As shown, the G and D band FWHM, as well as the Id/Ig band intensity ratios decreases with the heat treatment temperature, which indicate an increasing degree of graphitization of the Co-containing carbonaceous materials with temperature, in spite of their much more developed porosity. These results confirms that Cobalt may induce or promote certain structural ordering around the cobalt NPs, as suggested for other Co-containing carbon catalyst at temperatures above 450 ºC [23,64]. For example, the Co@CF-800 exhibited the lowest D and very low G band FWHM, which indicates that it has the highest degree of graphitization among all investigated samples and is consistent with the TEM results reported above. However, the Id/Ig ratio value for Co@CF-800 was not lower than those of other investigated Cobalt-containing graphitized carbon materials prepared at similar temperatures [23]. The degree of structural order on these samples is inferior to those reported for Co-containing carbon materials derived from the pyrolysis of Co-MOFs prepared at the same temperature [23,64]. On the other hand, Co@CF-500 exhibited very high G and D band FWHM, which indicates that it has a particularly low degree of graphitization and is consistent with the XRD result and the relatively high oxygen reactivity (rapid oxidation by oxygen) shown by this sample in an air TGA (Fig. S5). These results suggest that the high oxygen content incorporated to the lignin fiber during the stabilization step may hinder to some extent the graphitization on this type of Co-containing carbon samples, due to the self-oxidation and carbon gasification favored with increasing temperature (Fig. 1).

From the XPS, XRD, TEM and RAMAN results, it is clear that at the higher heat treatment temperature studied relatively more cobalt particles seems to be embedded in the carbon matrix and surrounded by graphitic-type carbon, which would prevent these cobalt particles from being easily exposed to any (reaction) gas atmosphere. Therefore, the formation of graphitic carbon layers could reduce the exposition of the

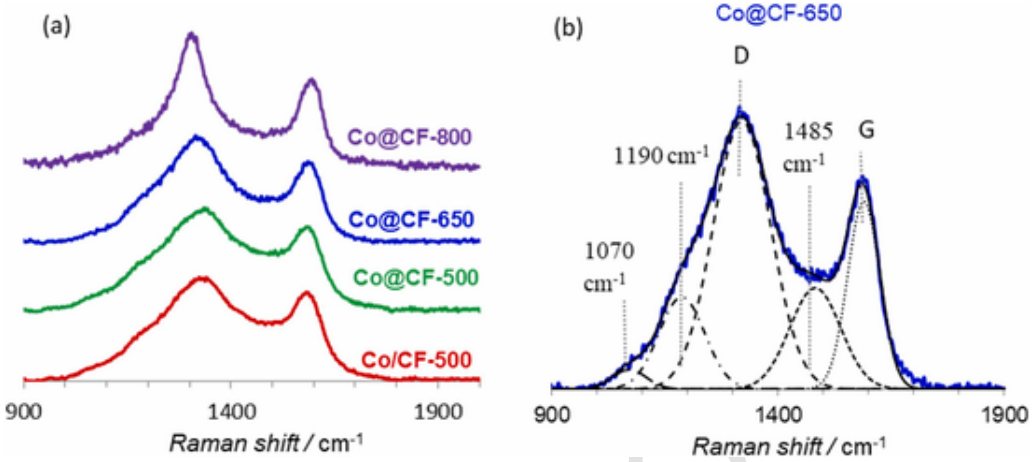

Fig. 7. First-order Raman spectra of the Cobalt-containing carbon fiber catalysts excited at 488 nm wavelength (a) and representative Raman spectra of Co@CF-650 showing the deconvolution (b).

cobalt active sites to syngas and would reduce the FTS activity of this catalyst (Co@CF-800).

Fig. 8 shows the H_2-TPR profiles for the Co-containing carbon fiber catalysts before H_2 reduction. The hydrogen consumption observed at temperatures between 190 °C and 375 °C is associated to the reduction of Co_3O_4 to metallic cobalt, which takes place through intermediate formation of CoO [12,69]. The lower reduction peaks observed for Co@CF-650 and Co@CF-800 catalysts within that temperature range may indicate that most of the cobalt on these samples are already in the metallic form, in agreement with the XPS and XRD results. A second and broad hydrogen reduction peak is exhibited from 375 to 700 °C by all the catalysts, which might correspond, on the one hand, to some gasification of the carbonaceous support to CH_4 and, on the other hand, to some reduction of oxygen-containing functional groups existing on the catalysts carbon surface [13]. Fig. S6 shows the MS signals of H_2O, CO, CO_2 and CH_4 obtained for the gases from Co@CF-500 during the H_2-TPR experiment and reveals the high formation of CH_4 above 375 °C. Moreover, metallic cobalt species are well known catalyst for the gasification reaction of carbon to methane [12,15]. The fact that cobalt is supported mainly on the most external surface of the carbon fibers determines the extent of carbon gasification during the H_2-TPR in the case of Co/CF-500, which is lower than in the case of Co@CF-500, where cobalt is distributed in the internal and external carbon fiber surface. This is evidenced by the lower amount of hydrogen consumed at temperatures above 375 °C during the H_2-TPR for Co/CF-500 compared to that for Co@CF-500 (Fig. 8) and by the lower MS signals of CH_4 measured during the TPR experiments (Fig. S6). On the contrary, the higher content and dispersion of cobalt observed for Co@CF-500 may produce a higher catalytic gasification of the carbon fibers by metallic cobalt than in the case of Co/CF-500, with lower cobalt content and dispersion. On the other hand, the TPD analysis for the Co-containing carbon catalysts (Fig. S7) indicates the presence of carbon-oxygen groups of acidic (carboxylic, lactonic) and non-acidic (carbonyl, ether, quinone and phenol) character on the Co-containing carbon catalysts surface, which evolve as CO_2 and CO, respectively, during the TPD experiment [70]. Moreover, it is clear that the amount of oxygen functional groups decreases with the heat treatment temperature caused by a deeper decomposition of these groups from the carbon catalyst surface. In fact, it is remarkable the greatly lower amount of H_2 consumed at higher temperatures (> 375 °C) in the case of Co@CF-800 catalyst caused by the lower concentration of oxygen surface groups that might be reduced on this sample and also to a possible reduction of the catalytic gasification of the carbon surface by a less reactive encapsulated metallic cobalt. Furthermore, the presence of cobalt oxides, which might be reduced at higher temperatures, should not be discarded, given that cobalt oxide species have also been reported to be reduced at temperatures around 430 °C on carbon supports, which depends on catalysts preparation, composition and dispersion [12,17]. As a reference, the degree of reduction, calculated as the ratio between the H_2 consumption from the first reduction peak up to 350 °C and the corresponding theoretical value, is 78% for Co@CF-500 (assuming all Co atoms to be initially in the form of Co_3O_4).

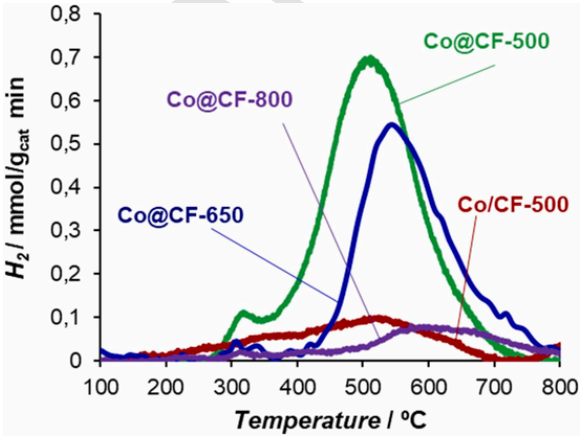

Fig. 8. H_2-TPR profile of the Co-containing CFs catalysts from 100 to 800 ºC.

3.3. Catalytic performance in Fischer-Tropsch synthesis

The catalytic activity of the Co-containing carbon fibers materials was assessed in the Fischer Tropsch synthesis process under different reaction conditions. Table 4 summarizes the FTS CO conversion, CTY, carbon selectivity to different product ranges and the olefin to paraffin ratio values after 70 h on-stream. Fig. 9 presents the evolution of CTY for the Co@CF catalysts obtained at different heat treatment temperatures as a function of the time-on-stream (TOS) at 240 ºC, a H_2/CO ratio of 1 and a GHSV of 4 $m^3_{STP}\ kg_{cat}^{-1}\ h^{-1}$. For the sake of comparison, Fig. S8 shows the evolution of CTY as a function of TOS for Co/CF-500 at a GHSV of 3.3 $m^3_{STP}\ kg_{cat}^{-1}\ h^{-1}$. The CTY remained stable above 5 h and up to 70 h TOS for all the catalysts, demonstrating the high stability of these Co@CF catalysts. The initial decay in CTY observed during the first 5 h TOS is a typical reversible deactivation of cobalt based catalysts caused by build-up of hydrocarbons and pore plugging [71]. However, the steady state CTY value decreases considerable with the increase of the heat treatment temperature for the obtained catalysts. For instance,

Table 4
CO conversion, activity per gram of Co (CTY) and carbon selectivity to products of FTS over Co-containing lignin carbon fibers after 70 h on stream at 20 bar total pressure and different temperature, feed composition H_2/CO ratios and space velocities.

no.	Catalyst	Process conditions			X_{CO} (%)	CTY (10^{-5} mol_{CO} g_{Co}^{-1} s^{-1})	TOF[a] (10^{-2} s^{-1})	S[b] (%)				O/P (C2-C4)
		T (ºC)	H_2/CO	GHSV (m^3_{STP} kg_{cat}^{-1} h^{-1})				C1	C2-C4	C5+	CO_2	
1	Co@CF-500	240	1	4	19.7	7.84	4.6	17.1	14.1	66.4	2.5	1.8
2	Co@CF-650	240	1	4	12.1	4.21	3.8	47.3	16.5	33.9	4.7	1.2
3	Co@CF-800	240	1	4	10.5	1.62	3.6	49.3	17.4	28.4[c]	4.9	1.0
4	Co/CF-500	240	1	3.3	9.9	6.07	6.6	22.8	17.9	55.7[c]	3.6	2.2
5	Co@CF-500	240	1	3.3	23.6	7.83	4.6	16.7	13.2	67.4	2.6	1.7
6	Co@CF-500	240	1	5.3	14.8	7.82	4.6	19.1	14.7	63.5	2.7	2.0
7	Co@CF-500	240	1	8	9.9	7.93	4.7	21.2	16.7	57.3	4.7	2.3
8[d]	Co@CF-500	220	1	3.3	9.4	2.69	1.60	12.1	10.5	75.4[c]	2.1	2.2
9[d]	Co@CF-500	220	2	3.3	14.2	2.75	1.63	22.4	16.2	59.6	2.3	1.4

[a] apparent turnover frequency (TOF, mol CO converted per mol of active Co atoms per second).
[b] Selectivities are lumped in methane (C1), short chain C2 to C4 hydrocarbons (C2-C4), long chain hydrocarbons with 5 or more carbon atoms (C5 +) and carbon dioxide (CO_2).
[c] The C5 + selectivity was calculated from the CO conversion by subtracting the fraction of CO used for the formation of C1 to C4 products, as determined via online GC, from the total amount of CO converted.
[d] Entries 8 and 9 were tested for 24 h TOS.

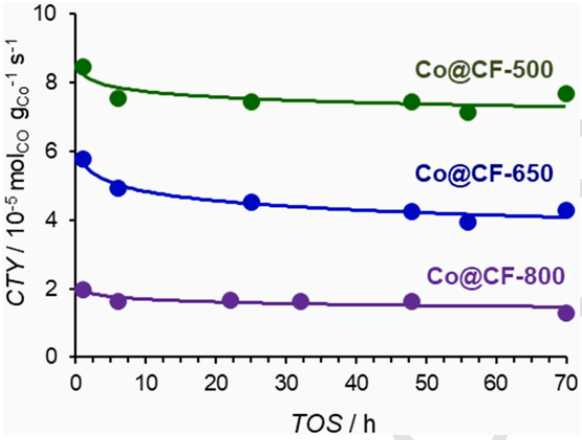

Fig. 9. CTY as a function of TOS during FTS at 240 °C, 20 bar, H_2/CO = 1 and GHSV = 4 $m^3_{STP,CO}$ kg_{cat}^{-1} h^{-1}.

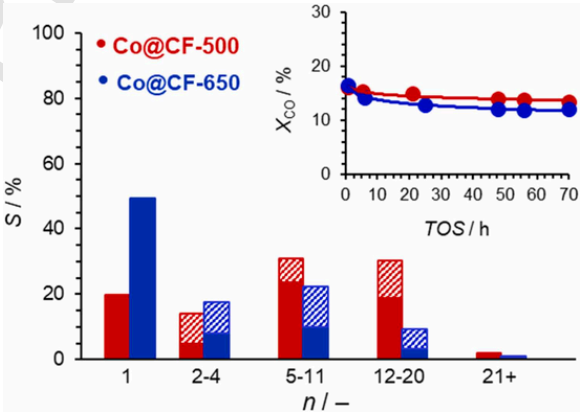

Fig. 10. Carbon selectivity toward products (with different number of carbon atoms) of FTS at iso-conversion conditions after 70 h on stream at 240 °C, 20 bar, H_2/CO = 1 for Co@CF-650 (GHSV = 4 m^3_{STP} kg_{cat}^{-1} h^{-1}) and (GHSV = 5.3 m^3_{STP} kg_{cat}^{-1} h^{-1}) for Co@CF-500. In each carbon number group from left to right: Co@CF-500 and Co@CF-650; ▉: n-paraffins, ///: sum of isoparaffins and olefins. Insert shows the CO conversion evolution as a function of time-on-stream (*TOS*).

the CTY value decreases by a factor of 5 over Co@CF-800 compared to that of Co@CF-500 (Table 4). The average size of the cobalt crystallites of the Co@CF samples increased with the heat treatment temperature (Figs. 5 and 6). Therefore, the lower CTY for Co@CF-650 and − 800 may be attributed to both the lower dispersion of the cobalt active phase and the formation of graphitic carbon structures encapsulating the active sites at high heat treatment temperatures (> 500 ºC), as evidenced by the XRD, TEM and RAMAN results (Figs. 5–7), which render them inaccessible for FTS [23,72]. The catalytic activities expressed as mole of CO converted per mole of surface cobalt active sites per second (TOF) was calculated using the dispersion values obtained from H_2 chemisorption. The TOF values decreases with the heat-treatment temperature from $4.6{\cdot}10^{-2}$ to $3.6{\cdot}10^{-2}$ s^{-1} for Co@CF-500 and Co@CF-800, respectively.

The carbon selectivity to the different hydrocarbon product ranges over Co@CF-500 and Co@CF-650 (entries nº 2 versus nº 6 in Table 4) is compared in Fig. 10 at *iso*-conversion conditions (as depicted in the figure inset). Under the applied reactions conditions, Co@CF-500 presents a relatively high selectivity to the gasoline-range (C5-C11, 31%) and diesel-range (C12-C20, 30%) hydrocarbons and the selectivity to waxes (C20 +) and methane (C1) is 1.6% and 19%, respectively. On the other hand, the production of methane significantly increases over Co@CF-650–47%, which is undesirable for FTS, while the selectivity to long chain hydrocarbons (C5 +) decreases to 34%. Moreover, this catalyst presents a selectivity to C2-C4 of 16.6%, slightly higher than that obtained for Co@CF-500, 14%. The selectivity towards CO_2 is very low for all the catalysts (Table 4), evidencing a very low water-gas shift activity under the applied reaction conditions, as expected for Co catalysts.

The CTY, TOF and the selectivity over Co/CF-500 and Co@CF-500 are also compared at iso-conversion conditions (entries 4 and 7, Table 4). Note that, the CTY and the selectivity to C5+ for Co@CF-500 are slightly higher than those for Co/CF-500, whereas the TOF value is higher for Co/CF-500. This can be ascribed to the different sizes and locations of the cobalt NPs on these two catalysts. For Co@CF-500, the cobalt NPs are located on the whole surface of the fiber structure (internal and external), while for Co/CF-500, most of the cobalt are located on the outmost external fiber surface (Table 3). The reaction intermediates that are formed inside the carbon fiber pores have longer residence time that those formed on the external carbon fiber surface because of the larger transfer resistance, which is favorable for both the CO conversion and the chain growth to form heavy hydrocarbons. Similar results were observed for cobalt nanoparticles supported on the surface and interior of carbon nanotubes [12,17]. In addition to this, as illustrated by XRD results and the cobalt particle size histograms (Figs. 5

and 6, respectively), the effect of the carbon matrix covering the cobalt NPs facilitate the dispersion of cobalt, given that smaller Co NPs were observed on Co@CF-500 than on Co/CF-500, which could contribute to the higher CTY of Co@CF-500. Therefore, the better FTS performance observed for Co@CF-500 can be attribute to a better dispersion of the active phase in the whole fiber surface and to an optimal metal Co NP size.

Co@CF-500 catalyst was also tested at different GHSV values (entries 1, 5, 6 and 7 in Table 4) and the carbon selectivity to the different hydrocarbon product ranges is plotted in Fig. S9. The CH_4 selectivity decreases and the C5+ selectivity increases as the CO conversion is increased. This increase in C5+ selectivity with the CO conversion is in line with previous studies and was attributed to secondary reactions of primary olefins at higher residence times [73] and to the increase in the partial pressure of water, which is suggested to inhibit secondary hydrogenation of primary olefins [74].

Table 4 also shows the effect of temperature and H_2/CO ratio on the selectivity of FTS products at steady state conditions (after 24 h TOS) over Co@CF-500 catalyst. Comparison of the hydrocarbon product distributions at 240 and 220 ºC and an H_2/CO ratio of 1 at iso-conversion conditions (entries 7 vs 8) clearly demonstrates that product distribution shows a shift to long-chain hydrocarbons (C5 +) at lower temperature. The selectivity to C5 + products for Co@CF-500 at 220 and 240 ˚C are 75.4% and 57.3%, respectively, whereas the selectivity to methane are 12.1 and 21.2, respectively. On the other hand, the olefin to paraffin ratio of the C2-C4 hydrocarbons remains constant at iso-conversion conditions (O/P-2.3). The results of Table 4 also show that the selectivity to C5 + decreases from 75.4% to 59.6% with increasing the H_2/CO ratio from 1 to 2 (entries 8 vs 9) at 220 ºC. The amount of adsorbed CO on catalyst surface is reduced by decreasing the partial pressure of CO, which will decrease the chain growth and increase the termination reaction to paraffins [17]. The results in Table 4 confirms that the amount of olefin to paraffin ratio is decreased from 2.2 to 1.4 with increasing the H_2/CO ratio from 1 to 2.

The production of methane is strongly influenced by the metal particle size during FT reaction when Co is used as the active metal. According to the literature, the catalytic activity and selectivity to long-chain hydrocarbons are maximized when metallic cobalt nanoparticles are in the order of 8 ± 2 nm either over oxides, carbon nanofibers (Co/CNF) and carbon (Co@C) catalyst supports [5,6,16,23,75–77]. Smaller cobalt NPs usually presented a large fraction of low-coordinated surface active sites, which decreased the surface coverages of the CH_x, OH_x and CO intermediates and increased the H coverage to a large extent, producing a high methane selectivity [5,77]. Therefore, we attribute the superior activity and low methane selectivity of Co@CF-500 catalyst to the optimal Co particle size observed from TEM, between 9 and 11 nm (mostly in form of Co_3O_4 according to XPS an XRD), which upon reduction would yield optimal metallic cobalt crystallites size between 6.8 and 8.3 nm, respectively ($d(Co^0) = 0.75(Co_3O_4)$) [64]. On the other hand, it was reported in the literature that the selectivity to methane, C2-C4 and C5+ remained constant with increasing the metallic cobalt particle size from 8 to 50 nm over Co/CNT, Co/CNF and Co@C catalysts [5,16, 23,75]. On the contrary, a greatly increase in the selectivity to methane is obtained with increasing the metallic cobalt crystallites size, as for Co@CF-650 and – 800, at iso-conversion conditions (entries 2, 3 and 7 in Table 4). In order to prove the absence of diffusional effects over the Co-containing carbon fibers, the internal pore diffusional limitation was estimated according to Weisz-Pratter criterion (C_{wp}), whereas the external mass transfer resistance was investigated through Carberry number analysis (Ca) [78,79]. Both criteria are defined in supporting information and the C_{wp} and Ca parameters are summarized in Tables S4 and S5. The results indicate that the internal and external mass transfer resistance are negligible. Also the heat transfer could be taken as negligible given the high dispersion of the metal active phase throughout the carbon fiber and catalyst bed and to the appropriate testing conditions, such as low reactor diameter (4 mm i.d.), low conversion levels and small temperature gradients along the bed (high quality furnace) [78]. Therefore, as the amount of adsorbed hydrogen over the catalyst surface is of primary importance in determining the selectivity to methane [77], the presence of graphitic carbon shells over the metallic cobalt sites and the narrower pores formed over Co@CF-650 and Co@CF-800 is expected to influence the adsorption behavior of H_2 over the active sites with respect to CO and thus contribute to a higher H coverage on the metallic active sites and methane selectivity.

A second aspect to be considered is that the olefin to paraffin ratio (O/P) of the C2-C4 hydrocarbons decreases with an increase in the heat treatment temperature. For instance, the O/P ratio is the highest over Co@CF-500 and decreases by a factor of 1.7 for Co@CF-650, under iso-conversion conditions (entries 2 and 6 in Table 4). Similar results were obtained by Luo et al. for FTS over Co-C catalysts obtained by pyrolyzing ZIF-67 MOF from 450 to 900 ºC [23]. Higher constraints in transport and higher α-olefin hydrogenation activity for Co@CF-650 and – 800 catalysts may account for these results. At the same time, it is observed that the O/P (C2-C4) ratio obtained over Co@CF-500 catalysts at different GHSV values is strongly dependent on CO conversion (entries 1, 5, 6 and 7 in Table 4), with O/P ratios at higher CO conversion levels. This has been attributed to the higher extent of α-olefin readsorption at lower space velocities, in spite of the higher water concentrations reducing the degree of secondary hydrogenation at higher conversions [80].

Fig. 11 depicts the selectivity distribution of liquid hydrocarbons (Fig. 11a) as well as the molar fraction distribution (Fig. 11b) of FTS products produced after 70 h on-stream for Co@CF-500 at 240 ˚C, H_2/CO ratio of 1 and GHSV of 3.3 m^3_{STP} kg_{cat}^{-1} h^{-1}. This sample shows a Gaussian type distribution centered between C9 and C11 (Fig. 11a), similar to that reported in the literature over Co@C [25], Co@CMK-3 [19] and Co/CNT [12,17] catalysts. The molar fraction of the FTS hydrocarbons versus their carbon number (Fig. 11b) follows a linear

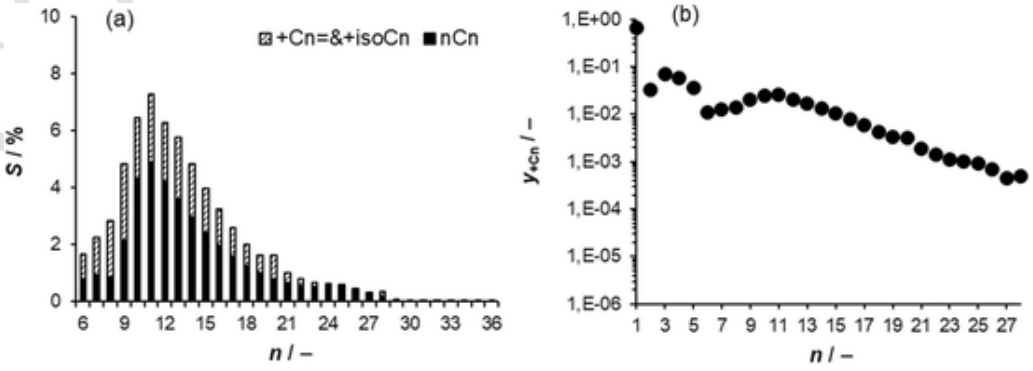

Fig. 11. Selectivity distribution of liquid hydrocarbons formed over Co@CF-500 (a) and chain growth probability (α = 0.80) obtained from the ASF plot in the C10-C28 hydrocarbon range. Liquid products were collected after 70 h on stream at 240 ˚C, 20 bar, H_2/CO = 1 and GHSV = 3.3 m^3_{STP} kg_{cat}^{-1} h^{-1}.

trend representative for an ASF distribution with a chain growth probability (α) of 0.80, lower value was obtained at 220 ºC and H_2/CO = 2 (α = 0.75). These α values are within the range of α values reported in the literature for Co catalysts supported on inorganic supports (α = 0.7–0.94) [72,81,82] and on carbo-based materials (α = 0.57–0.87) [7] for LT-FTS. Table S3 compares the FTS performance of Co@CF-500 (entries 1–4) with some of the most relevant and recent results reported in the literature using cobalt catalyst supported on carbon-based materials [7], such as Co/AC (entries 5–8), Co/MC (entry 9), Co/CNT (entries 10–12), Co/CNF (entries 13–15) and Co@C catalysts derived form MOFs (entries 16–19) and the benchmark catalyst, which is Co supported on SiO_2 prepared by incipient wetness impregnation (entry 20). In a work by Gascon et al. [72], highly loaded silica-supported cobalt Fischer–Tropsch catalysts (50 *wt.* % Co) were developed from ZIF-67 (entry 20) showing outstanding performance in the LTFTS. In this case, the Co@SiO_2-873 catalyst reached 16% of CO conversion and 90.5% of C5 + selectivity at 210 °C, 20 bar, H_2/CO ratio of 1 and a GHSV of 48 $m^3\ kg_{Co}^{-1}\ h^{-1}$. Although the conversions and selectivity values reported in the literature were obtained under different reaction conditions and metal loadings, as a general observation, it can be stayed that the performance of the Co@CF-500 catalyst falls within the expected values for improved LT-FTS catalysts reported in the literature. Noteworthy, TOF values in this work are in line to those over Co/AC (activated carbons), Co/OMC (ordered mesoporous carbons) and Co@C obtained from the pyrolysis of MOFs (Table S3) [7].

On the other hand, the decrease of CTY was negligible from 10 h up to 70 h TOS (Fig. 9), thus the stability of these Co@CFs catalysts is reasonably high, superior to that of other cobalt catalysts supported on carbon materials, such as that of Co/CNF [5,16,83] and cobalt supported on ordered mesoporous carbons [19]. This can be explained due to the spatial confinement effect of the porous carbon fiber matrix surrounding the metallic cobalt NPs, which prevents cobalt particles from sintering for long reaction times. In addition to this, the presence of surface oxygen functional groups on the carbon fibers, originated directly from the thermal treatment of the lignin fibers (without a prefunctionalization stage), may stably anchor the metallic cobalt sites and contribute to the high catalyst stability. In fact, Fig. S7 presents the evolution of CO and CO_2 in temperature-programmed desorption (TPD) experiments of the fresh catalysts, which evidences a high concentration of oxygen functional groups, particularly for those prepared at low heat treatment temperatures (Co@CF-500 and Co/CF-500), which decomposed as CO (from anhydride, carbonyl, ether, quinone and phenol surface groups) and/or CO_2 (from carboxylic, lactonic, anhydride ones) during the TPD. In this sense, Chernyak et al. [84] reported that quinones and phenols surface groups remained stable on the surface of CNTs after 70 h of FTS reaction at 190 °C, 1 bar, H_2/CO of 2 and SV of 2.2 $m^3 kg_{cat}^{-1} h^{-1}$, preventing Co from sintering during the catalytic reaction, given that the catalysts were not deactivated with TOS. On this context, the heat treatment of Co-based MOFs under an inert atmosphere has recently been demonstrated as a promising route to prepare highly loaded Co@C catalyst (30–50 *wt%* Co) with controllable cobalt particle size and high catalytic stability[64,85]. However, these type of catalysts show low activity and C5 + selectivity along with a high CH_4 selectivity in the FTS process when they are compared to Co@CF-500 catalyst [85]. In addition, Co@C catalysts derived from the heat treatment of MOFs have demonstrated to have a very low mechanical resistance for FTS [86]. The inferior performance of these MOF-derived pyrolyzed catalysts can be ascribed to the inaccessibility of most cobalt nanoparticles, which are encapsulated by graphitic shells from lower heat treatment temperatures (450 ºC) [64].

3.4. Co-containing carbon fibers catalysts after FTS reaction

The samples used in the FTS were characterized in order to further study the stability and morphology of these catalytic materials under FTS reaction conditions (240 °C, 20 bar, H_2/CO ratio of 1 and GHSV of 4 $m^3_{STP}\ kg_{cat}^{-1}\ h^{-1}$). The TGA analysis of the catalysts before and after reaction are showed in Fig. S5. As observed, the TGA profiles of the fresh and used samples are very similar, indicating that the carbonaceous support was not significantly gasified under the activation conditions (H_2 reduction) used in the present work neither during the FTS reaction. Additionally, these results confirm that the catalysts are not deactivated due to carbon deposition after 70 h TOS, since there is not variation in the carbon content. It is also noteworthy that higher heat treatment temperatures enhanced the oxidation onset temperature of the Co-containing carbon fibers despite the higher porosity and higher cobalt content, pointing to a higher graphitization degree of the carbon fiber structure with temperature. This is in agreement with the Raman spectra results. Therefore, these results also confirm the presence of graphitic carbon layers surrounding the metallic cobalt sites when the catalyst is pyrolyzed at high temperatures (> 500 °C), reducing the gas accessibility to the catalytic metallic cobalt sites either for carbon oxidation (TGA) or for FTS.

SEM micrographs of the used Co@CF-500, Co@CF-650 and Co/CF-500 samples, showed in Fig. 12, provide evidence of a population of CFs with diameters between 0.2 and 2.0 μm, similar to those of the fresh samples. Although some flatted and broken fibers are observed after reaction, this has been caused by the manipulation of the fibrillar catalysts in the unloading of the reactors. These results suggest that Co-containing carbon catalysts in a fibrillar morphology prepared in a single step by electrospinning of cobalt and lignin solutions and pyrolyzed at 500 ºC offers good mechanical resistance and heat and mass transfer for FTS. Furthermore, from the TEM image of the used Co@CF-500 catalysts (Fig. S10), Co NPs sizes uniformly distributed can be observed, with an overage metallic cobalt particle size of 7.4 ± 0.5 nm, similar to that expected from the reduction of the fresh catalyst Co@CF-500 (Fig. 6a,b). Therefore, it can be concluded that the sintering of metallic cobalt NPs over Co@CF catalysts during 70 h TOS in FTS is negligible.

4. Conclusions

In this paper, a simple and versatile method is presented to prepare low-cost cobalt-containing lignin-based carbon fibers catalysts for Low-Temperature Fischer-Tropsch synthesis (LTFTS). The method involves the electrospinning of Cobalt nitrate/lignin/ethanol solutions into submicro-sized Cobalt-containing lignin fibers in a single step, where

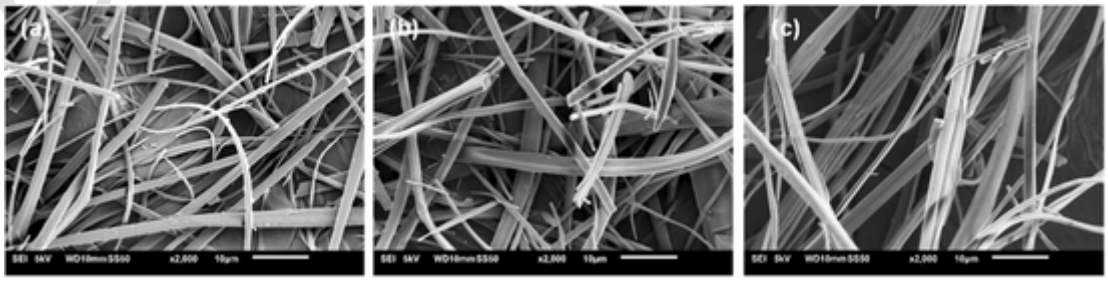

Fig. 12. SEM images of Co@CF-500 (a), Co@CF-650 (b) and Co/CF-500 after FTS reaction.

cobalt is deposited on the external surface or on the overall fiber surface (internal and external), depending if the Co precursor was pumped through the inner or the outer needle in the electrospinning step. Porous carbon fibers were obtained by a rapid oxidative treatment in air at 200 ˚C, to stabilize the Co-containing lignin fibers, followed by a heat treatment step in inert atmosphere at 500, 650 and 800 ˚C. The obtained flexible and porous fibrillar catalysts were tested for Low-Temperature FTS at 20 bar with an H_2/CO ratio comparable to that of the syngas obtained from the gasification of biomass (H_2/CO = 1) at 240 ˚C and with H_2/CO ratios of 1 and 2 at 220 ˚C. The fiber diameter size distribution for the bare carbon fiber was in the range of 1–4 μm, whereas a narrower diameter size range were obtained for the Co-containing carbon fiber catalysts (0.25–1 μm). When cobalt is located on the overall fiber surface (internal and external) the spatial confinement of the metallic Co nanoparticles in the porous carbon matrix allowed to reach a high dispersion of the Co species. In this sense, the catalysts pyrolyzed at 500 ˚C showed the best catalytic performance after 70 h on stream, with 75% and 60% selectivity to long chain hydrocarbons (C5+) at 220 ˚C and H_2/CO ratios of 1 and 2, respectively, which falls into the expected values found in the literature for LTFTS. Carbon fibers with a wider porosity allowed a higher cobalt dispersion accompanied with a wider porosity, and an optimal cobalt particle size, thus enabling a better accessibility of the cobalt particles to the reactant gases. These main catalytic properties explain the higher activity of Co@CF-500 for LTFTS. Higher heat treatment temperatures (> 500 ˚C) leads to the formation of cobalt nanoparticles encapsulated by graphitic-carbon shells, decreasing the LTFTS performance of these catalysts carbonized samples due to the inaccessibility of most cobalt nanoparticles.

CRediT authorship contribution statement

M.J. Valero-Romero : Writing – review & editing, Writing – original draft, Conceptualization, Investigation, Formal analysis. **F.J. García-Mateos :** Writing – review & editing, Investigation, Formal analysis. **Freek Kapteijn :** Writing – review & editing, Resources, Funding acquisition. **J. Rodríguez-Mirasol :** Writing – review & editing, Conceptualization, Resources, Funding acquisition. **T. Cordero :** Writing – review & editing, Resources, Funding acquisition.

Declaration of Competing Interest

The authors declare that they have no known competing financial interests or personal relationships that could have appeared to influence the work reported in this paper.

Data availability

Data will be made available on request.

Acknowledgments

The authors gratefully acknowledge the support of the Spanish Ministry of Sciences and Innovation (Project RTI2018-097555-B-I00) and Junta Andalucía (UMA18-FEDERJA-110 and P18-RT-4592). MJVR acknowledges MICIU for her Juan de la Cierva-Incorporación postdoctoral fellowship (IJC2019-041222-I), and FJGM thanks Junta Andalucía for his postdoctoral fellowship (DOC_00834). Funding for open acces charge: Universidad de Málaga / CBUA.

Appendix A. Supplementary material

Supplementary data associated with this article can be found in the online version at doi:10.1016/j.apcatb.2022.122078.

References

[1] R. Luque, A.R. de la Osa, J.M. Campelo, A.A. Romero, J.L. Valverde, P. Sanchez, Design and development of catalysts for biomass-to-liquid-Fischer–Tropsch (BTL-FT) processes for biofuels production, Energy Environ. Sci. 5 (2012) 5186–5202.
[2] D.J. Roddy, Biomass in a petrochemical world, Interface Focus 3 (2013) 20120038-20120038.
[3] S.R. Deshmukh, A.L.Y. Tonkovich, J.S. McDaniel, L.D. Schrader, C.D. Burton, K.T. Jarosch, A.M. Simpson, D.R. Kilanowski, S. LeViness, Enabling cellulosic diesel with microchannel technology, Biofuels 2 (2011) 315–324.
[4] A. Barbier, A. Tuel, I. Arcon, A. Kodre, G.A. Martin, Characterization and catalytic behavior of Co/SiO2 catalysts: influence of dispersion in the Fischer–Tropsch reaction, J. Catal. 200 (2001) 106–116.
[5] G.L. Bezemer, J.H. Bitter, H.P.C.E. Kuipers, H. Oosterbeek, J.E. Holewijn, X. Xu, F. Kapteijn, A.J. van Dillen, K.P. de Jong, Cobalt particle size effects in the Fischer−Tropsch reaction studied with carbon nanofiber supported catalysts, J. Am. Chem. Soc. 128 (2006) 3956–3964.
[6] G. Prieto, A. Martínez, P. Concepción, R. Moreno-Tost, Cobalt particle size effects in Fischer–Tropsch synthesis: structural and in situ spectroscopic characterisation on reverse micelle-synthesised Co/ITQ-2 model catalysts, J. Catal. 266 (2009) 129–144.
[7] M.J. Valero-Romero, M.Á. Rodríguez-Cano, J. Palomo, J. Rodríguez-Mirasol, T. Cordero, Carbon-based materials as catalyst supports for Fischer–Tropsch synthesis: a review, Front. Mater. 7 (2021).
[8] Y.-h Chin, J. Hu, C. Cao, Y. Gao, Y. Wang, Preparation of a novel structured catalyst based on aligned carbon nanotube arrays for a microchannel Fischer-Tropsch synthesis reactor, Catal. Today 110 (2005) 47–52.
[9] E. Asalieva, L. Sineva, S. Sinichkina, I. Solomonik, K. Gryaznov, E. Pushina, E. Kulchakovskaya, A. Gorshkov, B. Kulnitskiy, D. Ovsyannikov, S. Zholudev, V. Mordkovich, Exfoliated graphite as a heat-conductive frame for a new pelletized Fischer–Tropsch synthesis catalyst, Appl. Catal. A Gen. 601 (2020) 117639.
[10] L. Chen, G. Song, Y. Fu, J. Shen, The effects of promoters of K and Zr on the mesoporous carbon supported cobalt catalysts for Fischer–Tropsch synthesis, J. Colloid Interface Sci. 368 (2012) 456–461.
[11] H. Du, H. Zhu, Z. Zhao, W. Dong, W. Luo, W. Lu, M. Jiang, T. Liu, Y. Ding, Effects of impregnation strategy on structure and performance of bimetallic CoFe/AC catalysts for higher alcohols synthesis from syngas, Appl. Catal. A Gen. 523 (2016) 263–271.
[12] T. Fu, J. Lv, Z. Li, Effect of carbon porosity and cobalt particle size on the catalytic performance of carbon supported cobalt Fischer–Tropsch catalysts, Ind. Eng. Chem. Res. 53 (2014) 1342–1350.
[13] Y. Li, W. Lu, Z. Zhao, M. Zhao, Y. Lyu, L. Gong, H. Zhu, Y. Ding, Tuning surface oxygen group concentration of carbon supports to promote Fischer-Tropsch synthesis, Appl. Catal. A Gen. 613 (2021) 118017.
[14] H. Du, M. Jiang, H. Zhu, C. Huang, Z. Zhao, W. Dong, W. Lu, T. Liu, Z. Conrad Zhang, Y. Ding, Constructing efficient hcp-Co active sites for Fischer-Tropsch reaction on an activated carbon supported cobalt catalyst via multistep activation processes, Fuel 292 (2021) 120244.
[15] G.L. Bezemer, P.B. Radstake, U. Falke, H. Oosterbeek, H.P.C.E. Kuipers, A.J. van Dillen, K.P. de Jong, Investigation of promoter effects of manganese oxide on carbon nanofiber-supported cobalt catalysts for Fischer–Tropsch synthesis, J. Catal. 237 (2006) 152–161.
[16] G.L. Bezemer, P.B. Radstake, V. Koot, A.J. van Dillen, J.W. Geus, K.P. de Jong, Preparation of Fischer–Tropsch cobalt catalysts supported on carbon nanofibers and silica using homogeneous deposition-precipitation, J. Catal. 237 (2006) 291–302.
[17] M. Trépanier, A. Tavasoli, A.K. Dalai, N. Abatzoglou, Fischer–Tropsch synthesis over carbon nanotubes supported cobalt catalysts in a fixed bed reactor: influence of acid treatment, Fuel Process. Technol. 90 (2009) 367–374.
[18] Q. Chen, G. Liu, S. Ding, M. Chanmiya Sheikh, D. Long, Y. Yoneyama, N. Tsubaki, Design of ultra-active iron-based Fischer-Tropsch synthesis catalysts over spherical mesoporous carbon with developed porosity, Chem. Eng. J. 334 (2018) 714–724.
[19] X. Li, M.U. Nisa, Y. Chen, Z. Li, Co-based catalysts supported on silica and carbon materials: effect of support property on cobalt species and Fischer–Tropsch synthesis performance, Ind. Eng. Chem. Res. 58 (2019) 3459–3467.
[20] M.J. Valero-Romero, S. Sartipi, X. Sun, J. Rodríguez-Mirasol, T. Cordero, F. Kapteijn, J. Gascon, Carbon/H-ZSM-5 composites as supports for bi-functional Fischer–Tropsch synthesis catalysts, Catal. Sci. Technol. 6 (2016) 2633–2646.
[21] K. Cheng, V. Subramanian, A. Carvalho, V.V. Ordomsky, Y. Wang, A.Y. Khodakov, The role of carbon pre-coating for the synthesis of highly efficient cobalt catalysts for Fischer–Tropsch synthesis, J. Catal. 337 (2016) 260–271.
[22] C. Liu, Y. He, L. Wei, Y. Zhao, Y. Zhang, F. Zhao, S. Lyu, S. Chen, J. Hong, J. Li, Effect of TiO2 surface engineering on the performance of cobalt-based catalysts for Fischer–Tropsch synthesis, Ind. Eng. Chem. Res. 58 (2019) 1095–1104.
[23] Q.-X. Luo, L.-P. Guo, S.-Y. Yao, J. Bao, Z.-T. Liu, Z.-W. Liu, Cobalt nanoparticles confined in carbon matrix for probing the size dependence in Fischer-Tropsch synthesis, J. Catal. 369 (2019) 143–156.
[24] B. Qiu, C. Yang, W. Guo, Y. Xu, Z. Liang, D. Ma, R. Zou, Highly dispersed Co-based Fischer–Tropsch synthesis catalysts from metal–organic frameworks, J. Mater. Chem. A 5 (2017) 8081–8086.
[25] Y. Chen, X. Li, M.U. Nisa, J. Lv, Z. Li, ZIF-67 as precursor to prepare high loading and dispersion catalysts for Fischer-Tropsch synthesis: particle size effect, Fuel 241 (2019) 802–812.
[26] V.P. Santos, T.A. Wezendonk, J.J.D. Jaén, A.I. Dugulan, M.A. Nasalevich, H.-U. Islam, A. Chojecki, S. Sartipi, X. Sun, A.A. Hakeem, A.C.J. Koeken, M. Ruitenbeek,

T. Davidian, G.R. Meima, G. Sankar, F. Kapteijn, M. Makkee, J. Gascon, Metal organic framework-mediated synthesis of highly active and stable Fischer-Tropsch catalysts, Nat. Commun. 6 (2015) 6451.
[27] F. Rodríguez-reinoso, The role of carbon materials in heterogeneous catalysis, Carbon 36 (1998) 159–175.
[28] S. Aziz, K. Sarkanen, Organosolv pulping (a review), Tappi J. 72 (1989) 169–175.
[29] X. Pan, C. Arato, N. Gilkes, D. Gregg, W. Mabee, K. Pye, Z. Xiao, X. Zhang, J. Saddler, Biorefining of softwoods using ethanol organosolv pulping: preliminary evaluation of process streams for manufacture of fuel-grade ethanol and co-products, Biotechnol. Bioeng. 90 (2005) 473–481.
[30] F.J. García-Mateos, R. Ruiz-Rosas, J.M. Rosas, J. Rodríguez-Mirasol, T. Cordero, Controlling the composition, morphology, porosity, and surface chemistry of lignin-based electrospun carbon materials, Front. Mater. 6 (2019).
[31] J.M. Rosas, R. Berenguer, M.J. Valero-Romero, J. Rodríguez-Mirasol, T. Cordero, Preparation of different carbon materials by thermochemical conversion of lignin, Front. Mater. 1 (2014).
[32] M.J. Valero-Romero, E.M. Márquez-Franco, J. Bedia, J. Rodríguez-Mirasol, T. Cordero, Hierarchical porous carbons by liquid phase impregnation of zeolite templates with lignin solution, Microporous Mesoporous Mater. 196 (2014) 68–78.
[33] P.O. Ibeh, F.J. García-Mateos, J.M. Rosas, J. Rodríguez-Mirasol, T. Cordero, Activated carbon monoliths from lignocellulosic biomass waste for electrochemical applications, J. Taiwan Inst. Chem. Eng. 97 (2019) 480–488.
[34] J.M. Rosas, J. Bedia, J. Rodríguez-Mirasol, T. Cordero, HEMP-derived activated carbon fibers by chemical activation with phosphoric acid, Fuel 88 (2009) 19–26.
[35] Y. Matatov-Meytal, M. Sheintuch, Catalytic fibers and cloths, Appl. Catal. A Gen. 231 (2002) 1–16.
[36] M. Lallave, J. Bedia, R. Ruiz-Rosas, J. Rodríguez-Mirasol, T. Cordero, J.C. Otero, M. Marquez, A. Barrero, I.G. Loscertales, Filled and hollow carbon nanofibers by coaxial electrospinning of alcell lignin without binder polymers, Adv. Mater. 19 (2007) 4292–4296.
[37] F.J. García-Mateos, R. Berenguer, M.J. Valero-Romero, J. Rodríguez-Mirasol, T. Cordero, Phosphorus functionalization for the rapid preparation of highly nanoporous submicron-diameter carbon fibers by electrospinning of lignin solutions, J. Mater. Chem. A 6 (2018) 1219–1233.
[38] F.J. García-Mateos, T. Cordero-Lanzac, R. Berenguer, E. Morallón, D. Cazorla-Amorós, J. Rodríguez-Mirasol, T. Cordero, Lignin-derived Pt supported carbon (submicron)fiber electrocatalysts for alcohol electro-oxidation, Appl. Catal. B Environ. 211 (2017) 18–30.
[39] R. Ruiz-Rosas, J. Bedia, M. Lallave, I.G. Loscertales, A. Barrero, J. Rodríguez-Mirasol, T. Cordero, The production of submicron diameter carbon fibers by the electrospinning of lignin, Carbon 48 (2010) 696–705.
[40] I.G. Loscertales, J.E. Díaz Gómez, M. Lallave, J.M. Rosas, J. Bedia, J. Rodríguez-Mirasol, T. Cordero, M. Marquez, S. Shenoy, G.E. Wnek, T. Thorsen, A. Fernández-Nieves, A. Barrero, Coaxial electrospinning for nanostructured advanced materials, MRS Proc. 948 (2006) 0948-B0906-0901.
[41] F. Kapteijn, J.A. Moulijn, Structured catalysts and reactors – perspectives for demanding applications, Catal. Today 383 (2022) 5–14.
[42] J.F. Kadla, S. Kubo, R.A. Venditti, R.D. Gilbert, A.L. Compere, W. Griffith, Lignin-based carbon fibers for composite fiber applications, Carbon 40 (2002) 2913–2920.
[43] S. Kubo, Y. Uraki, Y. Sano, Preparation of carbon fibers from softwood lignin by atmospheric acetic acid pulping, Carbon 36 (1998) 1119–1124.
[44] R. Berenguer, F.J. García-Mateos, R. Ruiz-Rosas, D. Cazorla-Amorós, E. Morallón, J. Rodríguez-Mirasol, T. Cordero, Biomass-derived binderless fibrous carbon electrodes for ultrafast energy storage, Green Chem. 18 (2016) 1506–1515.
[45] S. Brunauer, P.H. Emmett, E. Teller, Adsorption of gases in multimolecular layers, J. Am. Chem. Soc. 60 (1938) 309–319.
[46] M.M. Dubinin, E.D. Zaverina, L.V. Radushkevich, Sorbtsiya I Struktura Aktivnykh Uglei.1. Issledovanie Adsorbtsii Organicheskikh Parov, Zh. Fiz. Khim. 21 (1947) 1351–1362.
[47] K. Kaneko, C. Ishii, Superhigh surface-area determination of microporous solids, Colloid Surf. 67 (1992) 203–212.
[48] J. Landers, G.Y. Gor, A.V. Neimark, Density functional theory methods for characterization of porous materials, Colloid Surf. A 437 (2013) 3–32.
[49] R.D. Jones, C.H. Bartholomew, Improved flow technique for measurement of hydrogen chemisorption on metal catalysts, Appl. Catal. 39 (1988) 77–88.
[50] S. Sartipi, H. Jansma, D. Bosma, B. Boshuizen, M. Makkee, J. Gascon, F. Kapteijn, Six-flow operations for catalyst development in Fischer-Tropsch synthesis: bridging the gap between high-throughput experimentation and extensive product evaluation, Rev. Sci. Instrum. 84 (2013).
[51] J.L. Braun, K.M. Holtman, J.F. Kadla, Lignin-based carbon fibers: oxidative thermostabilization of kraft lignin, Carbon 43 (2005) 385–394.
[52] C.J. Gómez, E. Mészáros, E. Jakab, E. Velo, L. Puigjaner, Thermogravimetry/mass spectrometry study of woody residues and an herbaceous biomass crop using PCA techniques, J. Anal. Appl. Pyrolysis 80 (2007) 416–426.
[53] H. Yang, R. Yan, H. Chen, D.H. Lee, C. Zheng, Characteristics of hemicellulose, cellulose and lignin pyrolysis, Fuel 86 (2007) 1781–1788.
[54] C.-W. Tang, C.-B. Wang, S.-H. Chien, Characterization of cobalt oxides studied by FT-IR, Raman, TPR and TG-MS, Thermochim. Acta 473 (2008) 68–73.
[55] Y. Yang, L. Jia, B. Hou, D. Li, J. Wang, Y. Sun, The oxidizing pretreatment-mediated autoreduction behaviour of cobalt nanoparticles supported on ordered mesoporous carbon for Fischer–Tropsch synthesis, Catal. Sci. Technol. 4 (2014) 717–728.
[56] J.L. Figueiredo, J. Rivera-Utrilla, M.A. Ferro-Garcia, Gasification of active carbons of different texture impregnated with nickel, cobalt and iron, Carbon 25 (1987) 703–708.
[57] G. Guan, M. Kaewpanha, X. Hao, A. Abudula, Catalytic steam reforming of biomass tar: prospects and challenges, Renew. Sustain. Energy Rev. 58 (2016) 450–461.
[58] W.K. Son, J.H. Youk, T.S. Lee, W.H. Park, The effects of solution properties and polyelectrolyte on electrospinning of ultrafine poly(ethylene oxide) fibers, Polymer 45 (2004) 2959–2966.
[59] D. Cazorla-Amorós, J. Alcañiz-Monge, A. Linares-Solano, Characterization of activated carbon fibers by CO_2 adsorption, Langmuir 12 (1996) 2820–2824.
[60] K.S.W. Sing, Reporting physisorption data for gas/solid systems with special reference to the determination of surface area and porosity (recommendations 1984), Pure Appl. Chem. 57 (1985) 603–619.
[61] X. Pan, X. Bao, Reactions over catalysts confined in carbon nanotubes, Chem. Commun. (2008) 6271–6281.
[62] Y. Brik, M. Kacimi, M. Ziyad, F. Bozon-Verduraz, Titania-supported cobalt and cobalt–phosphorus catalysts: characterization and performances in ethane oxidative dehydrogenation, J. Catal. 202 (2001) 118–128.
[63] V.I. Nefedov, M.N. Firsov, I.S. Shaplygin, Electronic structures of MRhO2, MRh2O4, RhMO4 and Rh2MO6 on the basis of X-ray spectroscopy and ESCA data, J. Electron Spectrosc. Relat. Phenom. 26 (1982) 65–78.
[64] X. Sun, A.I. Olivos-Suarez, L. Oar-Arteta, E. Rozhko, D. Osadchii, A. Bavykina, F. Kapteijn, J. Gascon, Metal–organic framework mediated cobalt/nitrogen-doped carbon hybrids as efficient and chemoselective catalysts for the hydrogenation of nitroarenes, ChemCatChem 9 (2017) 1854–1862.
[65] H. Zhang, C. Lancelot, W. Chu, J. Hong, A.Y. Khodakov, P.A. Chernavskii, J. Zheng, D. Tong, The nature of cobalt species in carbon nanotubes and their catalytic performance in Fischer–Tropsch reaction, J. Mater. Chem. 19 (2009) 9241–9249.
[66] F. Morales, E. de Smit, F.M.F. de Groot, T. Visser, B.M. Weckhuysen, Effects of manganese oxide promoter on the CO and H2 adsorption properties of titania-supported cobalt Fischer–Tropsch catalysts, J. Catal. 246 (2007) 91–99.
[67] A. Cuesta, P. Dhamelincourt, J. Laureyns, A. Martínez-Alonso, J.M.D. Tascón, Raman microprobe studies on carbon materials, Carbon 32 (1994) 1523–1532.
[68] A. Sadezky, H. Muckenhuber, H. Grothe, R. Niessner, U. Pöschl, Raman microspectroscopy of soot and related carbonaceous materials: spectral analysis and structural information, Carbon 43 (2005) 1731–1742.
[69] P. Arnoldy, J.A. Moulijn, Temperature-programmed reduction of CoOAI2O3 catalysts, J. Catal. 93 (1985) 38–54.
[70] J.L. Figueiredo, M.F.R. Pereira, M.M.A. Freitas, J.J.M. Órfão, Carbon 37 (1999) 1379.
[71] N.E. Tsakoumis, M. Rønning, Ø. Borg, E. Rytter, A. Holmen, Deactivation of cobalt based Fischer–Tropsch catalysts: a review, Catal. Today 154 (2010) 162–182.
[72] X. Sun, A.I.O. Suarez, M. Meijerink, T. van Deelen, S. Ould-Chikh, J. Zečević, K.P. de Jong, F. Kapteijn, J. Gascon, Manufacture of highly loaded silica-supported cobalt Fischer–Tropsch catalysts from a metal organic framework, Nat. Commun. 8 (2017) 1680.
[73] E. Iglesia, S.C. Reyes, R.J. Madon, S.L. Soled, Selectivity control and catalyst design in the Fischer-Tropsch synthesis: sites, pellets, and reactors, in: D.D. Eley, H. Pines, P.B. Weisz (Eds.), Advances in Catalysis, Academic Press, 1993, pp. 221–302.
[74] S. Storsæter, Ø. Borg, E.A. Blekkan, A. Holmen, Study of the effect of water on Fischer–Tropsch synthesis over supported cobalt catalysts, J. Catal. 231 (2005) 405–419.
[75] Z.-j Wang, S. Skiles, F. Yang, Z. Yan, D.W. Goodman, Particle size effects in Fischer–Tropsch synthesis by cobalt, Catal. Today 181 (2012) 75–81.
[76] Ø. Borg, P.D.C. Dietzel, A.I. Spjelkavik, E.Z. Tveten, J.C. Walmsley, S. Diplas, S. Eri, A. Holmen, E. Rytter, Fischer–Tropsch synthesis: cobalt particle size and support effects on intrinsic activity and product distribution, J. Catal. 259 (2008) 161–164.
[77] J.P. den Breejen, P.B. Radstake, G.L. Bezemer, J.H. Bitter, V. Frøseth, A. Holmen, K.P. de Jong, On the origin of the cobalt particle size effects in Fischer–Tropsch catalysis, J. Am. Chem. Soc. 131 (2009) 7197–7203.
[78] J.A. Moulijn, A. Tarfaoui, F. Kapteijn, General aspects of catalyst testing, Catal. Today 11 (1991) 1–12.
[79] H.S. Fogler, Elements of Chemical Reaction Engineering Prentice-Hall, New Jersey, 1999.
[80] S. Krishnamoorthy, M. Tu, M.P. Ojeda, D. Pinna, E. Iglesia, An investigation of the effects of water on rate and selectivity for the Fischer–Tropsch synthesis on cobalt-based catalysts, J. Catal. 211 (2002) 422–433.
[81] B. Jager, R. Espinoza, Advances in low temperature Fischer-Tropsch synthesis, Catal. Today 23 (1995) 17–28.
[82] D. Vervloet, F. Kapteijn, J. Nijenhuis, J.R. van Ommen, Fischer–Tropsch reaction–diffusion in a cobalt catalyst particle: aspects of activity and selectivity for a variable chain growth probability, Catal. Sci. Technol. 2 (2012) 1221–1233.
[83] G.L. Bezemer, T.J. Remans, A.P. van Bavel, A.I. Dugulan, Direct evidence of water-assisted sintering of cobalt on carbon nanofiber catalysts during simulated Fischer–Tropsch conditions revealed with in situ mössbauer spectroscopy, J. Am. Chem. Soc. 132 (2010) 8540–8541.
[84] S.A. Chernyak, E.V. Suslova, A.S. Ivanov, A.V. Egorov, K.I. Maslakov, S.V. Savilov, V.V. Lunin, Co catalysts supported on oxidized CNTs: evolution of structure during preparation, reduction and catalytic test in Fischer-Tropsch synthesis, Appl. Catal. A Gen. 523 (2016) 221–229.
[85] K.O. Otun, X. Liu, D. Hildebrandt, Metal-organic framework (MOF)-derived catalysts for Fischer-Tropsch synthesis: recent progress and future perspectives, J. Energy Chem. 51 (2020) 230–245.
[86] L. Oar-Arteta, M.J. Valero-Romero, T. Wezendonk, F. Kapteijn, J. Gascon,

Formulation and catalytic performance of MOF-derived Fe@C/Al composites for high temperature Fischer–Tropsch synthesis, Catal. Sci. Technol. 8 (2018) 210–220.